Doctoral Thesis

Power and Signal Transmission Using Two-Dimensional Waveguide

(２次元伝送路による電力・信号伝送とその応用)

増田　祐一

Abstract

This thesis reports on a research project that aims to develop a high efficient and long distance wireless power transmission system using sheet-like medium. A moving object having a receiver can be charged just by passing over the sheet-like medium. The sheet-like medium is sufficiently longer than the target object such as an electric vehicle, an autonomous mobile robot, and a personal mobility. If all the routes of the moving object are covered with the sheet-like medium, the moving object can be charged anywhere. It is not necessary to go to the charging spot and it can keep moving for a long time.

Sheet-like medium guides electromagnetic waves and generates evanescent (non-radiative) field above its surface. And the receiver coupler loaded on the moving object can extract the electromagnetic waves through the sheet surface. This scheme was first proposed by Yamahira et al. 2006.

In this work, we point out the trade-off relationship between the transmission distance and efficiency when the coupler extracts power. And a sheet-like medium is designed to achieve high efficiency and the long transmission distance between the power source and coupler. The most important contribution of this work is to extend the transmission distance by developing a high-inductive surface sheet. Sufficient coupling strength between the sheet and the coupler can be achieved even if an operating frequency is 13.56 MHz industrial, scientific and medical (ISM) band. As a simulated result, 84 % theoretical limit of the power transmission efficiency is achieved with a transmission distance of 100-m.

This thesis also presents a following two research project based on the two-dimensional transmission line technology. The first one is a low power and high speed data transmission system in a room-scale two-dimensional communication (2DC) environment. The second one is a battery-less body sensor networks (BSN) based on a conductive thread embroidered fabric (CTEF) technology.

Contents

Part I

Wireless Power Transmission Using Sheet-like Waveguide

Chapter 1

Introduction

1.1   Wireless Power Transmission

Wireless Power Transmission (WPT) technology is desired for a moving object such as an electric vehicle, an autonomous mobile robot, and a personal mobility. Those moving objects require a large battery capacity and a long charging time, and it is a significant problem[1, 2]. WPT can reduce the cost of charging and reduce battery capacity. The operating time of moving objects will increase and the cost and weight will decrease.

The WPT to the moving object is classified into two types: WPT to an object in stopped and WPT to an object in moving. The former is effective for applications where the object periodically stops. For example, in the WPT to buses, charging while parking at each bus stop is effective for saving charging time and the battery capacity [3, 4, 5]. The latter is effective for applications that need to keep moving constantly. Ideally, sufficient power supply to the object in moving can eliminate the battery and it extends the operating time infinitely.

In WPT system design for the object in moving, the following factor should be considered:

- Long-distance : The cost of the WPT system decreases as the distance between a power source and a target device increases.
- Selectivity : The damage to the health of human and the interference to electronic devices have to be prevented.
- Efficiency : High-efficient WPT reduces the heating of equipment and realizes a greener system

Long-distance can reduce the cost of the WPT system for the following two reasons. One is that the power sources can be sparsely placed as the distance between the power source and the target device increase. The other one is that a sheet-like transmission medium shown in Fig.1.1 is low cost because it can be made of a metal thin film and an inexpensive dielectric material.

Actually, the methods for realizing long-distance and high-selectivity are the same.
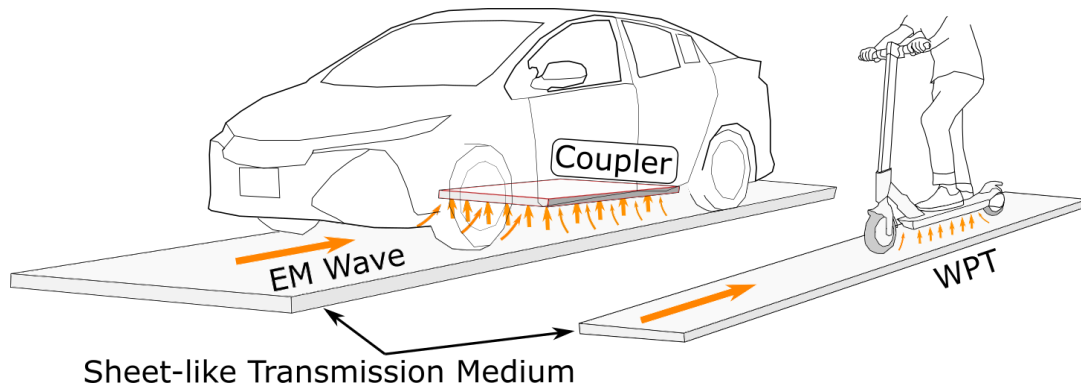
Figure1.1: An image of the WPT system using sheet-like medium. Each device can extract the power from the sheet-like medium by using receive coupler.

To realizes long-distance and high-selectivity, suppression of leakage EM field from the transmission medium is required. The propagation loss increases as the leakage EM field from the sheet-like transmission medium increase.

The selectivity can be increased by the following two factors: one is the suppression of EM field generated around transmitter, receiver and power transmission medium. Most of the EM field has to be trapped within these. The other one is the prevention of absorption of EM energy to objects other than target devices.

EM field with a frequency of 10 MHz or higher raises body temperature [6]. In this frequency range, exposure assessment is performed by using specific absorption rate (SAR) which is defined as the rate at which energy is absorbed per unit mass of body tissue. The reference value at each frequency is specified in ICNIRP (International Commission on Non-Ionizing Radiation Protection) Guideline 2010 and the WPT system have to keep this standard [6].

1.2 Motivation and Related Works

In this work, the feasibility of a WPT system that supplies power to a target object placed at 100-m away from the power source is verified. An image of the system is illustrated in Fig. 1.1. A linear sheet-like transmission medium is laid on the roadway and sidewalk. Because this medium is sufficiently longer than the electric vehicle or the electric kick scooter in the direction of travel, those object in moving can extract power from the medium anywhere on the route. And the sheet-like medium has a width enough to absorb lateral drift.

In this work, a WPT system which uses a sheet-like medium having inductive surface is exploited[7]. This system is different from conventional inductive/capacitive coupling in principle. The sheet-like medium guides electromagnetic waves and generates evanescent (non-radiative) field above its surface. The basic guided mode in the sheet is similar
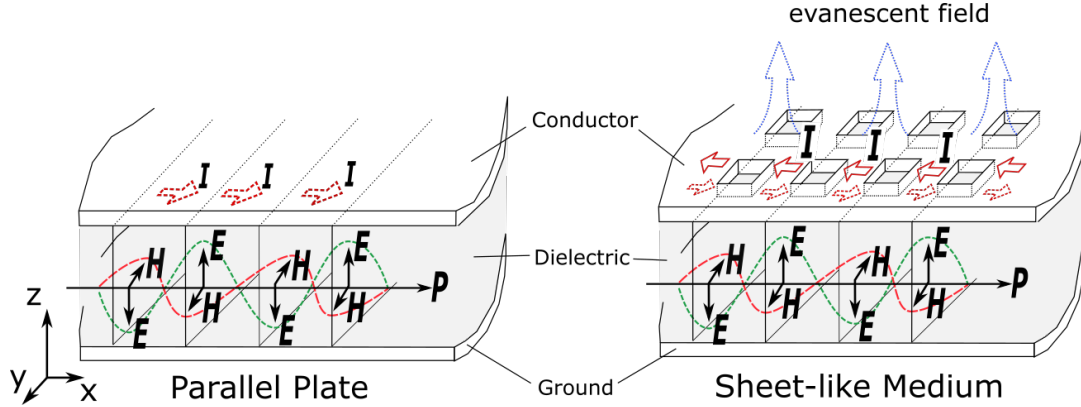
Figure1.2: Waveguide mode of the parallel plate (left side) and the sheet-like medium (right side). In the sheet-like medium, the conductor surface has a pattern structure. A current flow on the front side of the surface conductor. And it generates the evanescent field above on surface.

to that of the parallel plate shown on the left side of Fig. 1.2. The dielectric layer is sandwiched in the conductor layer. The surface conductor has a pattern structure. Therefore, a current also flows on the front side of the surface conductor and it generates the evanescent field. In this respect, it is different from a parallel plate. Special couplers on the sheet can extract microwave power from the sheet-like medium across the surface conductor.

The WPT is classified by the distance between the transmitter/transmission medium and the receiver. The microwave beam system can achieve the long-distance WPT [8, 9]. This system is suitable for applications where a line of sight between transmitter and receiver can be secured. For example, a drone in flight is an effective device as a power transmitter [10]. On the other hands, it is unsuitable in environments where transmission paths are frequently interrupted.

In the magnetic resonance coupling method, sufficient power can be transmitted with a distance larger than the coil diameter[11, 12, 13]. This method is suitable for applications where the moving object can be stopped on the coil embedded in the ground. Sufficient power can be transmitted from the coil embedded in the ground to the coil loaded on the bottom of the moving object. A kW class WPT with over 90% efficiency is reported in[3, 4, 5]. On the other hand, suppressing the EM field generated around the coil is a technical problem [4]. An electromotive force is generated when a strong magnetic field is applied to a loop conductor such as a necklace.

Close-range proximity WPT can reduce such a risk. The WPT using the sheet-like transmission medium corresponds to this. The strong EM field is generated into the close proximity space between the sheet-like medium and the coupler [7, 14, 15]. In other space where objects other than the power supply target (e.g. human, other electrical devices,
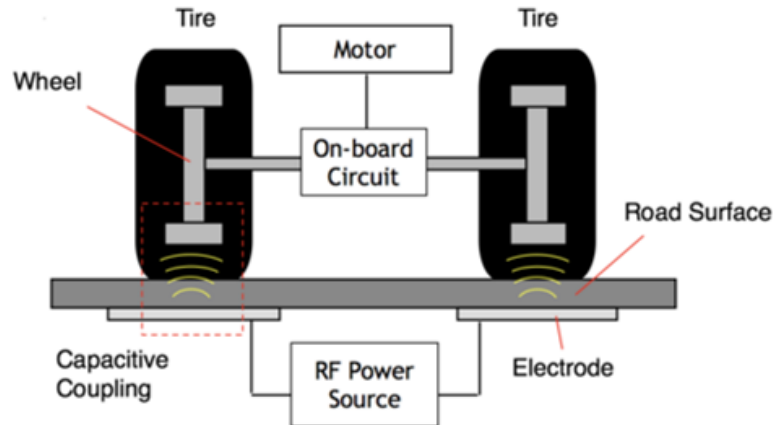
Figure1.3: Capacitive coupling system proposed in [19]. Most EM fields are trapped in tire rubber.

etc.) exist, sufficient weak EM fields are generated compared to the space between the sheet-like medium and the coupler.

The basic concept of a WPT system using inductive-surface sheet was originally published by Yamahira et al., in 2006 [16]. And the trade-off relationship between selectivity and efficiency is verified by Noda in 2012 [15]. And a prototype WPT system that has high selectivity and efficiency is proposed in the same thesis. In the previous works, the target devices are electronic devices placed on the desk, such as laptops and mobile phones. The 2.4 to 2.5-GHz industrial, scientific and medical (ISM) band is used.

Although the WPT system proposed in this work is based on the same technology, the operating frequency and the target device are different. The 13.56-MHz ISM band can be used. The structure of the sheet-like medium is simple and its manufacture cost is low. The thinness of the sheet-like medium is about 1-cm. Thus, it can be installed only by spreading a thin sheet-like medium on the ground. Simple work which is equivalent to carpet laying work can be expected.

Capacitive coupling between the electrode plate embedded in the road and the steel belt in the tire is another practical solution (Fig. 1.3) [17, 18, 19]. EM field leakage to the outside can be suppressed by confining the EM field in the tire rubber and road surface sandwiched between the electrodes. The EM field generated around the power transmission line, which is two conductor plates arranged in parallel, is different from that of the sheet-like medium. In the sheet-like medium, most of all the EM energy is confined in a dielectric sandwiched on the conductor plate.

In the previous works on the WPT using sheet-like medium, there was no discussion on the trade-off between transmission distance and efficiency when the coupler extract the power from the sheet-like medium. This thesis clarifies the relationship between
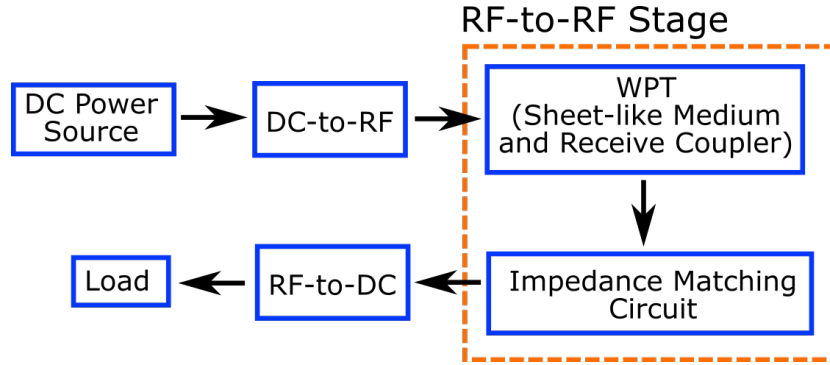
Figure1.4: Overview of WPT system.

transmission distance and efficiency, and presents the feasibility of long-distance and high-efficient WPT system.

1.3   Contributions and Outline

An overview of general WPT system is shown in Fig. 1.4. In this paper, the theoretical limit of the power transmission efficiency in RF-to-RF stage is estimated from the theoretical equation and the simulation result. The theoretical limit of the power transmission efficiency is defined as the efficiency when a coupler without a loss (e.g. conductor loss, radiation loss, etc.) is used. The design steps of the RF-to-RF stage are as follows:

1. Set numerical targets for transmission distance and power transmission efficiency.
2. Design the sheet-like medium and estimate the theoretical limit of the power transmission efficiency.
3. Design a coupler aiming at achieving the theoretical limit.

We set that the target value of the transmission distance is 100-m and the target value of the power transmission efficiency is 80% or more. The sheet-like medium and coupler are the most important factors in determining efficiency, transmission distance, and selectivity. One of the major contributions is to propose a new surface pattern of the sheet-like medium that has higher inductivity than the mesh structure which is used in previous works [7, 14]. And the design parameters of the sheet medium were set to optimum values. The target value can be achieved by using the new surface pattern. The operating frequency can be lowered to around 10 MHz.

Apart from the WPT system, we also propose an application using a sheet-like medium with a two-dimensional spread.

1.4   Organization

The organization of the thesis is following. Works on the WPT system are presented in Part 1, from Chapter 2 to Chapter 4. An application using a sheet-like medium with two-dimensional spread are presented in Part 2, from Chapter 5 to Chapter 6. The contents of part 2 are different from WPT.

In Chapter 2, each parameter of the sheet-like medium is formulated by EM field analysis of the sheet-like medium. Chapter 3 presents an equivalent circuit model that represents the relationship between the sheet-like medium and the receiving coupler. The power transmission efficiency is obtained from the circuit parameters, and the trade-off relationship between transmission distance and efficiency is explained. In Chapter 4, a high inductive surface pattern of the sheet-like medium is presented. In Part 2, high speed and low power consumption wireless data transmission is presented in Chapter 5. Chapter 6 shows the application of the energy harvesting and a battery-less body sensor networks by using a conductive thread embroidered fabric (CTEF) technology. Finally, we will conclude the thesis in Chapter 7.

Chapter 2

Sheet Parameter

In this chapter, sheet parameters, which is necessary for the discussion in Chapter 3 and later, are formulated. The sheet parameters are as follows: an attenuation constant in the direction along the sheet-like medium α, a surface impedance Z_0 and an inherent characteristic impedance R_{sx}.

The above parameters are obtained based on the EM field analysis of the waveguide mode of the sheet-like medium. Actually, the waveguide mode of the sheet-like medium was formulated in [15]. The process of those formulations is omitted as much as possible in order to focus on deriving sheet parameters.

2.1 Waveguide Mode

This section deals with EM field analysis of plane waves in order to understand the waveguide mode from the power source to the receiver. A cross-sectional model of the sheet-like medium is shown in Fig. 2.1. A dielectric layer is sandwiched between a ground conductor plane and a surface conductor layer. A Cartesian coordinate system is used, the x-axis is parallel to the direction of plane wave propagation, and the z-axis is perpendicular to the sheet plane.

2.2 EM Field Inside and Outside the Sheet

The two-dimensional distribution of the charge density ρ existing in the surface conductor and the current density i flowing in the surface conductor can be described as follows:
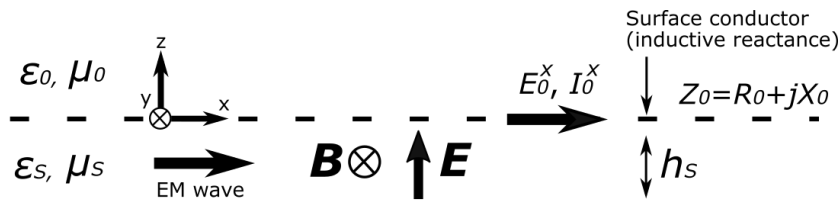

Figure2.1: Cross section model of the waveguide sheet.

$$\boldsymbol{i}(x, y) = \begin{pmatrix} I_0 \\ 0 \end{pmatrix} \exp{(jkx)}. \tag{2.1}$$

$$\rho(x, y) = \rho_0 \exp{(jkx)}. \tag{2.2}$$

Note that $\exp{(j\omega t)}$, which represents time-varying of EM field, is omitted.

The EM field is assumed that it is homogeneous with respect to the y-axis. And the current only flows with respect to the x-axis. k denotes the x-axis wavenumber. The waveguide mode is a transverse magnetic (TM) mode and is expressed as follows:

· inside sheet

$$\begin{pmatrix} E_x \\ E_y \\ E_z \end{pmatrix} = \begin{pmatrix} a \\ 0 \\ b \end{pmatrix} \exp{(-k_1 z)} \exp{(jkx)}, \quad \begin{pmatrix} B_x \\ B_y \\ B_z \end{pmatrix} = \begin{pmatrix} 0 \\ c \\ 0 \end{pmatrix} \exp{(-k_1 z)} \exp{(jkx)}, \tag{2.3}$$

· outside sheet

$$\begin{pmatrix} E_x \\ E_y \\ E_z \end{pmatrix} = \begin{pmatrix} d \sin{(k_2 z)} \\ 0 \\ e \cos{(k_2 z)} \end{pmatrix} \exp{(jkx)}, \quad \begin{pmatrix} B_x \\ B_y \\ B_z \end{pmatrix} = \begin{pmatrix} 0 \\ f \\ 0 \end{pmatrix} \cos{(k_2 z)} \exp{(jkx)}, \tag{2.4}$$

where k_1 and , k_2 denotes z-axis propagation constants of inside and outside sheet, respectively.

2.3   Boundary Conditions

I_0, a, b, c, d, e, f are formulated as a function of ρ_0 by using Maxwell's equation.

According to the charge conservation law $(-\partial\rho/\partial t = \mathrm{div}\boldsymbol{i})$, I_0 and ρ_0 satisfy the following equation.

$$-j\omega\rho_0 = jkI_0. \tag{2.5}$$

According to the Gauss's law $(\rho = \mathrm{div}\boldsymbol{D}$, where $\boldsymbol{D} \equiv \epsilon\boldsymbol{E})$, we obtain

$$b\epsilon_0 \exp{(-k_1 h)} - e\epsilon_S \cos{(k_2 h)} = \rho_0. \tag{2.6}$$

According to the Ampere's law $(\mathrm{rot}\boldsymbol{H} = \partial\boldsymbol{D}/\partial t + \boldsymbol{i}$, where $\boldsymbol{H} \equiv (1/\mu)\boldsymbol{B})$, in each area of the inside, outside, and their boundary, the following equation is obtained.

$$\text{(Boundary)} \quad c\frac{\exp{(-k_1 h)}}{\mu_0} - f\frac{\cos{(k_2 h)}}{\mu_S} = -I_0, \tag{2.7}$$

$$\text{(Outside)} \quad j\omega\epsilon_0 a = \frac{k_1}{\mu_0}c, \quad j\omega\epsilon_0 b = j\frac{k}{\mu_0}c, \tag{2.8}$$

$$\text{(Inside)} \quad j\omega\epsilon_S d = \frac{k_2}{\mu_S}f, \quad j\omega\epsilon_S e = j\frac{k}{\mu_S}f. \tag{2.9}$$

According to the Faraday's law $(\mathrm{rot}\boldsymbol{E} = -\partial\boldsymbol{B}/\partial t)$,

$$a \exp\left(-k_1 h\right) = d \sin\left(k_2 h\right). \tag{2.10}$$

The surface impedance is obtained by using Ohm's law.

$$Z_0 \equiv R_0 + jX_0 \equiv \frac{E_0^x}{I_0^x}. \tag{2.11}$$

Finally, from the wave equation, the EM wave propagating in the sheet-like medium satisfies the following Helmholtz equation:

$$k^2 - k_1^2 = \mu_0 \epsilon_0 \omega^2, \quad k^2 + k_2^2 = \mu_S \epsilon_S \omega^2. \tag{2.12}$$

The equations from (2.5) to (2.12) are all of the constraint condition.

Substituting (2.5), (2.6) and (2.8) into (2.11), we obtain

$$k_2 \sin\left(k_s h\right) \frac{1}{\cos\left(k_2 h\right) - \dfrac{\epsilon_0 k_2}{\epsilon_S k_1} \sin\left(k_2 h\right)} = jZ_0 \epsilon_S \omega. \tag{2.13}$$

Assuming $k_2 h \ll 1$ and $|\frac{\epsilon_0 k_2}{\epsilon_S k_1} \sin\left(k_2 h\right)| \ll 1$ and approximating the (2.13), we obtain

$$k_2^2 = \frac{jZ_0 \epsilon \omega}{h}. \tag{2.14}$$

And substituting (2.14) into (2.12), we obtain

$$k_1^2 = (\mu_S \epsilon_S - \mu_0 \epsilon_0)\omega^2 - \frac{jZ_0 \epsilon \omega}{h}, \quad k^2 = \mu_S \epsilon_S \omega^2 - \frac{jZ_0 \epsilon \omega}{h}. \tag{2.15}$$

The sheet parameters are obtained by using the above equations.

2.4　Sheet Parameter

2.4.1　Attenuation constant

The complex permittivity is defined as $\epsilon_S = \mathrm{Re}[\epsilon_S] - \mathrm{Im}[\epsilon_S] = \epsilon_{Sr} - j\epsilon_{Si}$. And the dielectric loss tangent is defined as $\tan\delta = \epsilon_{Si}/\epsilon_{Si}$. By using the complex permittivity and the dielectric loss tangent, wavenumber k is expressed as

$$k = \frac{2\pi}{\lambda_S}\sqrt{1 - j\tan\delta - j\frac{Z_0}{\mu_S \epsilon_{Sr} \omega}} \approx \frac{2\pi}{\lambda_S} - j\left(\frac{\pi}{\lambda_S}\tan\delta + \frac{\sqrt{\epsilon_{Sr}\mu_S}Z_0}{2\mu_S h}\right), \tag{2.16}$$

where λ_S is the wavelength of the plane wave in the sheet.

Since the imaginary term of the wavenumber k is the attenuation constant α, we obtain

$$\alpha = \frac{\pi}{\lambda_S} \tan\delta + \frac{R_0}{2h\sqrt{\mu_S/\epsilon_{Sr}}}. \qquad (2.17)$$

2.4.2 Surface impedance

The sheet surface resistance is expressed as

$$R_0 = \frac{\rho_S}{d_S}, \qquad (2.18)$$

where ρ_S and d_S represent the electrical resistivity and the skin depth, respectively. The skin depth is defined as $d_S = \sqrt{2\rho_S/\omega\mu_0}$.

Assuming $R_0 << X_0$, and substituting $Z_0 \approx jX_0$ and $k = 2\pi/\lambda_S$ into (2.15), the sheet surface reactance is expressed as

$$X_0 = \frac{(2\pi/\lambda_S)^2 - \omega^2\mu_S\epsilon_S}{\omega\epsilon_S/h}. \qquad (2.19)$$

2.4.3 Inherent characteristic impedance

Assuming that the EM field in the sheet is uniform, the inherent characteristic impedance is expressed as

$$R_{sx} = \frac{hE_z}{H_y} = h\mu_S\frac{e}{f} = h\frac{k}{\omega\epsilon_S} \qquad (2.20)$$

$$= \sqrt{\frac{\omega\mu_S h + X_0}{\omega\epsilon_S/h}}. \qquad (2.21)$$

2.5 Conclusion

In this chapter we obtain the attenuation constant in the direction along the sheet-like medium α, a surface impedance Z_0 and an inherent characteristic impedance R_{sx} from the EM field analysis. EM field analysis shows that the sheet surface impedance Z_0, which varies with sheet surface conductor pattern, determine the guided mode.

Chapter 3

Transmission Distance

In this chapter, the sheet-like medium and the receiving coupler are represented by an equivalent circuit. The relationship between the power transmission efficiency and each circuit parameter is clarified. A trade-off relationship between the propagation loss and the efficiency when the coupler extracts power from the sheet will be described.

3.1 Power Transmission Efficiency

Fig. 3.1 shows a cross-sectional view of the sheet-like medium and the receiving coupler. The power transmission efficiency is defined as

$$\eta = \frac{P_{out}}{P_{sup}}. \tag{3.1}$$

Let d_{cp} be the distance from the power source to the edge of the coupler, P_{in} is expressed as

$$P_{in} = P_{sup} \exp\left(-2\alpha d_{cp}\right), \tag{3.2}$$

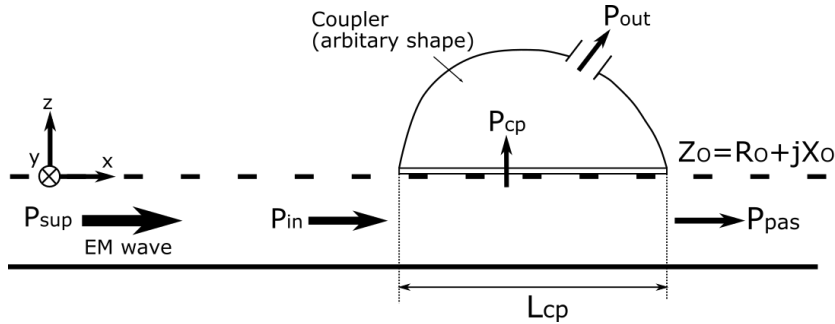where the attenuation constant α is formulated in (2.17).

Figure3.1: Cross section model of the sheet-like medium and the receiving coupler. P_{sup} denotes the power supplied in the sheet. P_{in} and P_{pas} denotes the power flowing inside the sheet at the edge of the coupler on -x side and +x side, respectively. P_{cp} denotes the power extracted to the coupler. P_{out} denotes the power supplied to the load.

we define the efficiency when the coupler extracts power from the sheet as η_{cp}. And it is expressed by the following equation.

$$\eta_{cp} = \frac{P_{out}}{P_{in}}. \tag{3.3}$$

Substituting (3.6) and (3.3) into (3.1), we obtain

$$\eta = \eta_{cp} \exp\left(-2\alpha d_{cp}\right). \tag{3.4}$$

η_{cp} and $\exp\left(-2\alpha d_{cp}\right)$ are in a trade-off relationship. η_{cp} will be formulated by using the sheet parameters obtained in Chapter 2. After this, we will discuss this trade-off relationship.

3.2   Equivalent Circuit

In this Section, an equivalent circuit that replace Fig. 3.1 will be proposed.

The advantage of representing Fig. 3.1 in the equivalent circuit is shown below.

- The trade-off relationship can be expressed easily.
- The power transmission efficiency of the entire WPT system including the impedance matching circuit, the impedance of the source and load can be discussed.
- The discussion is simpler than the EM field analysis.

In the section 3.2.1, (3.4) will be represented by the following three key parameters. One is the Q value of the sheet surface, the other is the coupling strength between the sheet and the coupler, and finally the attenuation constant in the sheet.

The Q value determines how much heat loss of surface conductor occurs when the coupler extracts EM power. The coupling strength determines how much the coupler can extract the EM power flowing in the sheet. The attenuation constant determines how much propagation loss occurs from the power source to the coupler. Those three key parameters can express the trade-off relationship between η_{cp} and $\exp\left(-2\alpha d_{cp}\right)$.

Fig. 3.2 shows that the equivalent circuit representing a region other than the coupler in Fig. 3.1. The voltage source and source impedance installed at the edge of the coupler on -x side equivalently replaces the P_{in} shown in Fig. 3.1.

Supposing that the source voltage in Fig. 3.2 is v_{in} and the current flowing through the power source impedance Zs is i_{in}, P_{in} is expressed as follows.

$$P_{in} = \frac{1}{2}\mathrm{Re}\left[v_{in}i_{in}^{*}\right], \tag{3.5}$$
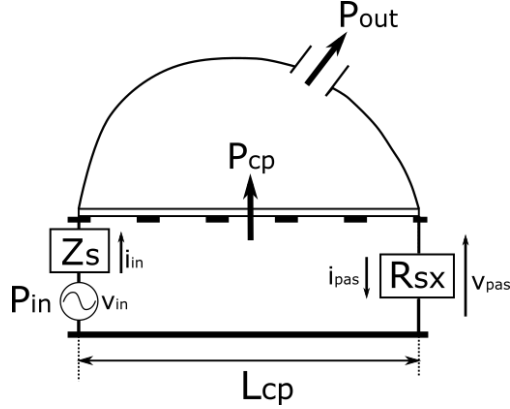
Figure3.2: Equivalent circuit representing a region other than the coupler
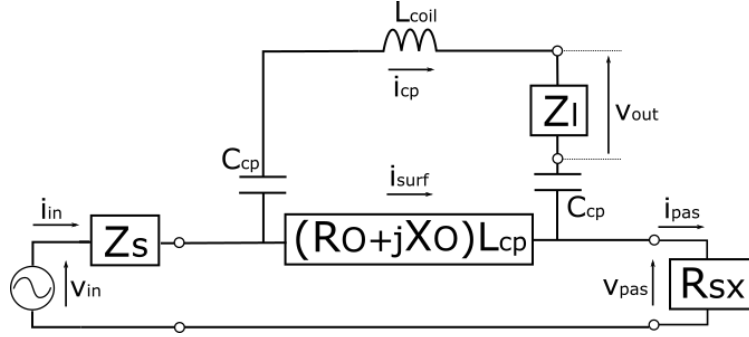

Figure3.3: Equivalent circuit including receiving coupler.

note that: $*$ represents a complex conjugate.

And P_{pas} is expressed as follows.

$$P_{pas} = \frac{1}{2}\mathrm{Re}\left[\mathrm{v_{pas}i_{pas}^*}\right], \tag{3.6}$$

where v_{pas} and i_{pas} denotes the voltage applied to both ends of R_{sx} and the current flowing through R_{sx} respectively. R_{sx} denotes the impedance that equivalently represents the +x side from the edge of the coupler on +x side.

The receiving coupler is represented by an equivalent circuit as shown in Fig. 3.3.

As a coupling method of the sheet and the coupler, a magnetic/electric field coupling method or a method using both of them can be considered. In this work, we will assume an electric field coupling method. The coil loaded in the coupler cancels the reactance between the coupler electrode and the surface conductor. Thus, this coil means an impedance matching circuit.

Assuming that L_{coil} always satisfies the following equation, Fig. 3.3 is simplified to Fig. 3.4.
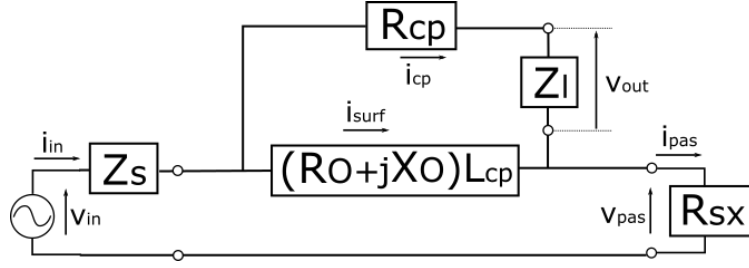
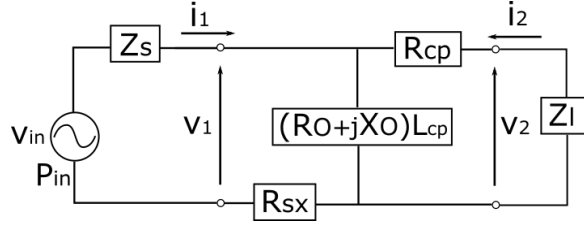Figure3.4: Equivalent circuit in the case where impedance matching is achieved.

Figure3.5: Circuit rewritten in Fig. 3.4 as a 2-port circuit.

$$\omega L_{coil} = \frac{1}{2\omega C_{cp}} \tag{3.7}$$

ω denotes the angular frequency of the electromagnetic wave propagating in the sheet.

Assuming that the Q value of the coil is Q_{cp}, R_{cp} shown in Fig. 3.4 is expressed by the following equation.

$$R_{cp} = \frac{\omega L_{coil}}{Q_{cp}} = \frac{1}{2\omega C_{cp}Q_{cp}} \tag{3.8}$$

R_{cp} represents the loss of the impedance matching circuit.

3.2.1 Power transmission efficiency

Fig. 3.5 shows a two-port circuit from a power source to a load. In [20], a method for calculating maximum power transmission efficiency in a two-port circuit has been proposed. In this section, by using this method, we derive the maximum power transmission efficiency with an optimum impedance of source and load.

In Fig. 3.5, η_{cp} which is defined in (3.3) is expressed as

$$\eta_{cp} = -\frac{i_2 v_2^*}{i_1 v_1^*}. \tag{3.9}$$

v_1, i_1, v_2, i_2 and impedance matrix $\mathbf{Z}$ satisfy the following relationship.

$$\begin{bmatrix} v_1 \\ v_2 \end{bmatrix} = \begin{bmatrix} Z_{11} & Z_{21} \\ Z_{21} & Z_{22} \end{bmatrix} \begin{bmatrix} i_1 \\ i_2 \end{bmatrix} \tag{3.10}$$

Here, the impedance matrix $\boldsymbol{Z}$ is as follows.

$$\begin{bmatrix} Z_{11} & Z_{21} \\ Z_{21} & Z_{22} \end{bmatrix} = \begin{bmatrix} R_{11} & R_{21} \\ R_{21} & R_{22} \end{bmatrix} + j \begin{bmatrix} X_{11} & X_{21} \\ X_{21} & X_{22} \end{bmatrix} \tag{3.11}$$

$$= \begin{bmatrix} R_0 L_{cp} + R_{sx} & R_0 L_{cp} \\ R_0 L_{cp} & R_0 L_{cp} + R_{cp} \end{bmatrix} + j \begin{bmatrix} X_0 & X_0 \\ X_0 & X_0 \end{bmatrix} \tag{3.12}$$

η_{cp} is maximized when the impedance of the power source Z_S and the load Z_l satisfy the following equation.

$$Z_S^* = Z_{in} = \frac{v_1}{i_1} = Z_{11} + Z_{21} \frac{i_2}{i_1} \tag{3.13}$$

$$= Z_{11} - Z_{12} \frac{Z_{21}^2}{Z_l + Z_{22}}, \tag{3.14}$$

$$Z_l^* = Z_{out} = \frac{v_2}{i_2} = Z_{22} + Z_{21} \frac{i_1}{i_2} \tag{3.15}$$

$$= Z_{22} - Z_{12} \frac{Z_{21}^2}{Z_s + Z_{11}}, \tag{3.16}$$

where Z_{in} and Z_{out} respectively denotes the impedance when viewing the right side from the power supply and the impedance when looking at the left side from the load.

By solving simultaneous equations of (3.14) and (3.16), we obtain

$$\begin{bmatrix} Z_S \\ Z_l \end{bmatrix} = \begin{bmatrix} R_S \\ R_l \end{bmatrix} + j \begin{bmatrix} X_S \\ X_l \end{bmatrix} \tag{3.17}$$

$$= \begin{bmatrix} \sqrt{D}/(R_0 L_{cp} + R_{cp}) \\ \sqrt{D}/(R_0 L_{cp} + R_{sx}) \end{bmatrix} + j \begin{bmatrix} R_0 X_0 L_{cp}^2/(R_0 L_{cp} + R_{cp}) - X_0 L_{cp} \\ R_0 X_0 L_{cp}^2/(R_0 L_{cp} + R_{sx}) - X_0 L_{cp} \end{bmatrix}, \tag{3.18}$$

where

$$D = \left(|\boldsymbol{R}| + R_0^2 L_{cp}^2 + X_0^2 L_{cp}^2 \right) |\boldsymbol{R}| \tag{3.19}$$

$$|\boldsymbol{R}| = R_0 L_{cp} R_{sx} + R_0 L_{cp} R_{cp} + R_{sx} R_{cp}. \tag{3.20}$$

v_1, i_1, v_2, i_2 can be obtained from Z, Z_S and Z_l. Substituting them into (3.9), we obtain the following maximum efficiency.

$$\eta_{cp} = 1 + \frac{2}{R_0^2 L_{cp}^2 + X_0^2 L_{cp}^2} \left\{ |\boldsymbol{R}| - \sqrt{D} \right\} \tag{3.21}$$

3.3   Trade-off Relationship

In this section, (3.21) is simplified by using efficiency angle θ [20]. The trade-off relationship between η_{cp} and the propagation loss is discussed.

The efficiency angle θ is defined by the following.

$$\tan 2\theta = \frac{\sqrt{(R_0^2 + X_0^2)L_{cp}^2}}{\sqrt{|\mathbf{R}|}} \approx \sqrt{Q_0 \zeta}, \tag{3.22}$$

where

$$Q_0 \equiv \frac{X_0}{R_0}, \quad \zeta \equiv \frac{X_0 L_{cp}}{R_{sx}}. \tag{3.23}$$

The loss of the impedance matching circuit does not contribute to the trade-off relationship. In order to simplify the expression, $\mathbf{R}_{cp}$ is assumed to be 0. And we also assume $R_0^2 << X_0^2$ in (3.22).

In (3.23), Q_0 denotes the Q value of the sheet surface and ζ denotes the coupling strength between the sheet and the coupler. By using this efficiency angle θ, (3.4) is modified to the following equation.

$$\eta = \tan^2\theta \cdot \exp\left(-2\alpha d_{cp}\right) \tag{3.24}$$

As $\tan 2\theta$ increases from 0 to infinity, $\tan^2\theta$ increases from 0 to 1 accordingly. In order to increase efficiency, the efficiency angle θ have to increase. Simultaneously, the attenuation constant α have to decrease.

Developing a surface conductor pattern with high inductivity that can realize sufficient X_0 even at low frequencies is effective. At low frequencies, R_0 decrease as the in-sheet wavelength λ_S increase. Thus, it can decrease α while maintaining sufficient Q_0 and ζ.

Next, the relationship between each parameter and efficiency will be discussed.
Surface Resistance R_0:   When the R_0 decreases, Q_0 increases and α decreases. Thus, η increases. Using conductors with high conductivity is effective.
Surface Reactance X_0:   As the X_0 increases, Q_0 and α increases simultaneously. It means that X_0 can only be increased to the range that propagation loss is allowed.
Characteristic Impedance R_{sx}:   Let the inductance of the sheet surface be L_0, R_{sx} is corrected to the following equation.

$$R_{sx} = \sqrt{\frac{\omega\mu_S h + \omega L_0}{\omega\epsilon_S/h}} = \sqrt{\frac{\mu_S h + L_0}{\epsilon_S/h}} \tag{3.25}$$

As the R_{sx} decreases, the ζ increases. Thus, ζ increase as the sheet becomes thin. On the other hand, because alpha also increases, the sheet can only be thinned to the range that the propagation loss is allowed. Similarly to the thickness, ζ and the propagation loss have a trade-off relationship even in the dielectric constant.

Coupler Length L_{cp}:   Increasing L_{cp} is effective if it is acceptable. This parameter does not affect Q_0 and α.

3.4   Verification of the Accuracy

This section shows that the accuracy of (3.24) is verified using the efficiency formulated from EM field analysis as a comparison target. The efficiency formula, which is presented in [15], is expressed as

$$\eta_{EM} = \phi(rm) \cdot \psi(rm), \tag{3.26}$$

$$\phi(rm) \equiv 1 - Q_0^{-1}(rm + rm^{-1}), \tag{3.27}$$

$$\psi(rm) \equiv 1 - \exp\left(-\zeta rm\right). \tag{3.28}$$

Considering the propagation loss, (3.26) is expressed as follows.

$$\eta_{EM} = \phi(rm) \cdot \psi(rm) \cdot \exp\left(-2\alpha d_{cp}\right). \tag{3.29}$$

rm is the ratio of the magnetic field strength between inside and outside the sheet. The efficiency which can not be exceeded in every *rm* is taken as the maximum efficiency and it is shown in Fig. 3.6. Efficiency obtained from (3.24) is also plotted at the same graph. (3.29) is the most exactly for calculating the maximum efficiency.

Note that the parameters used for the calculation are the same. The sheet parameters shown in Table 4.1 and Table 4.2 in Chapter 3 are used.

In Fig. 3.6, an error of up to 10% has occurred. But the frequencies at which the efficiency peaks are nearly the same. Thus, (3.24) can use for searching for optimum sheet parameters.

3.5   Conclusion

In this chapter, the relationship between the sheet and the coupler was expressed by an equivalent circuit, and the power supply efficiency was obtained. And we revealed the trade-off relationship between the propagation loss and the efficiency when the coupler extracts power flowing in the sheet. Finally, we verified the accuracy of the formula obtained from the equivalent circuit.

The theoretical analysis revealed that developing a surface conductor pattern with high inductivity that can realize sufficient X_0 even at low frequencies is required.
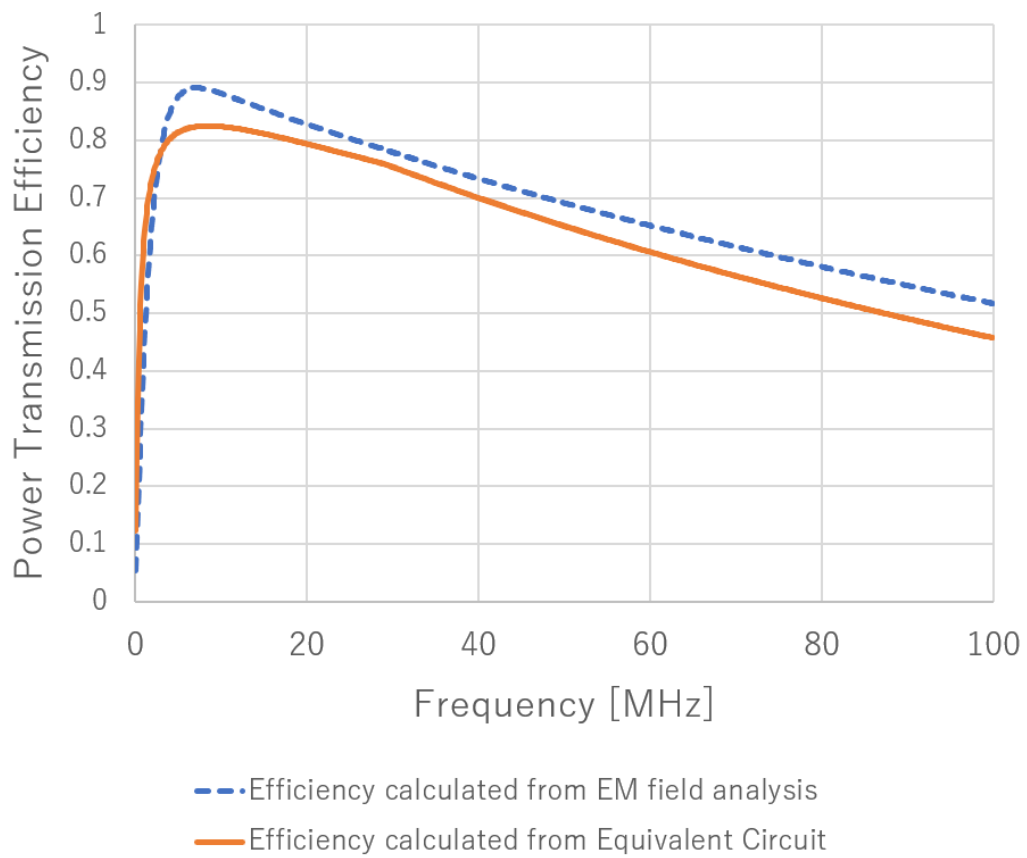
Figure3.6: Comparison of estimated efficiency.

Chapter 4

High-Inductive Surface Sheet

As described in the previous chapter, lowering the operating frequency is effective for long distance transmission. To realize that, a sheet surface pattern with high inductance is required. In this chapter, we propose a sheet surface pattern that can realize sufficient reactance at 13.56 MHz ISM band as the target frequency.

Next, based on the efficiency equation and the simulated result, the optimum sheet parameter, which maximizes the efficiency, will be determined.

4.1　High-Inductive Surface Conductor Pattern

In the previous work of the WPT system using the sheet-like medium, a mesh pattern as shown in Fig. 4.1 (a) has been used for the sheet surface pattern. As a matter of fact, a sufficient reactance cannot be realized at 13.56 MHz for the mesh structure. To solve this problem, we propose a high-inductive surface pattern as shown in Fig. 4.1 (b). By using this structure, the efficiency calculated from (3.24) becomes over 80% where the transmission distance is 100-m and the operating frequency is 13.56MHz.

4.1.1　Concept

In order to realize higher inductance than the mesh pattern, we propose a surface pattern of a zigzag structure shown in Fig. 4.1(b). The current flowing through the surface conductor and the magnetic field generated around the conductor are shown in Fig. 4.1(c) (d).

In the case of the mesh pattern, the directions of the currents flowing through the adjacent conductors are the same. The magnetic fields generated by them cancel out each other. On the other hand, in the zigzag pattern, the magnetic fields strengthen because the direction of the current is different. Thus, stronger inductivity than mesh sheet can be realized.
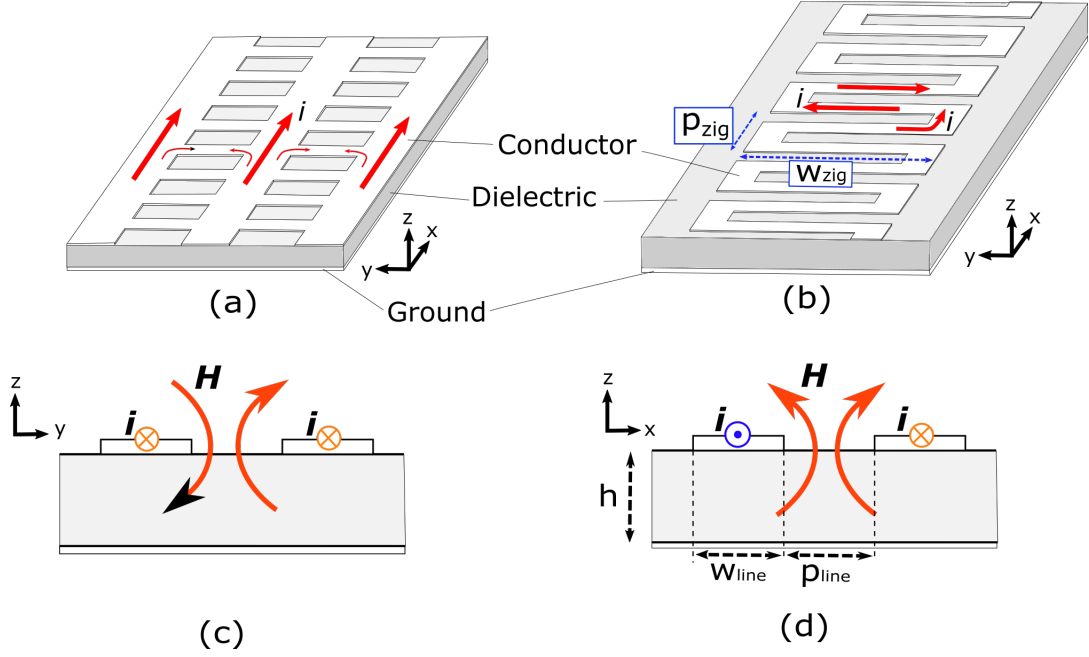
Figure4.1: Surface conductor pattern and the magnetic field formed around the conductor. (a) mesh pattern, (b) ZigZag pattern, (c) the magnetic fields generated by adjacent conductors cancel each other, (d) The magnetic fields generated by adjacent conductors strengthen each other.

4.1.2   Design basis of sheet

The two design parameters in the zigzag sheet are the following: one is the width of the zigzag pattern w_{zig}, the other one is the sheet thickness h. The surface inductance is determined by the ratio of w_{zig} to p_{zig}. However, if w_{zig} is increased, the necessary conductors per unit length in the x-direction are lengthened. Thus, surface resistance increase. In the zigzag sheet, (2.18) is modified as

$$R_0 \approx \frac{w_{zig}}{p_{zig}} \frac{\rho_S}{d_S}, \tag{4.1}$$

In order to strengthen the magnetic field efficiently, a width of conductor line w_{line} and the spacing between conductors p_{line} should be the same value. When p_{line} is larger than h and w_{line}, the magnetic field does not strengthen in a sparse area as shown in Fig. 4.2 (b). When h is larger than w_{line}, and p_{line}, the magnetic field is concentrated above and below the surface as shown in Fig. 4.2 (c). Interference to the guided mode in the sheet decreases. Thus, h, w_{line} and p_{line} are set to the same value.

$$h = W_{line} = p_{line}$$

(a)

$$h = W_{line} < p_{line}$$
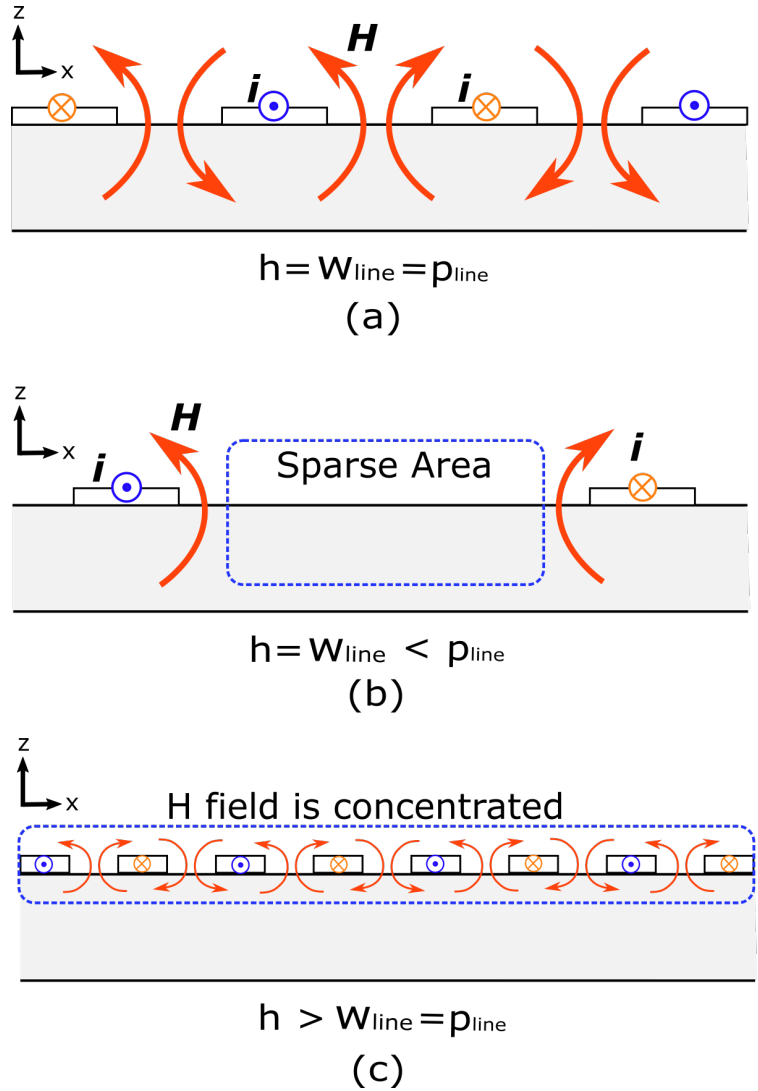
(b)

$$h > W_{line} = p_{line}$$

(c)

Figure4.2: Magnetic field generated around the conductor. (a) When h, w_{line}, and p_{line} have the same value, the magnetic field is most efficiently strengthened. (b) When p_{line} is larger than h and w_{line}, the magnetic field does not strengthen in a sparse area. (c) When h is larger than w_{line}, and p_{line}, the magnetic field is concentrated above and below the surface.

4.2   Full-Wave Simulation

This section presents an evaluation of the power transmission efficiency by various parameters. The maximum achievable efficiency can be evaluated.

The simulation model is shown in Fig. 4.3. The wavelengths in the sheet are calculated thorough 3D full-wave simulation using CST Microwave Studio. The sheet surface reactance is calculated by substituting the wavelength into (2.19).
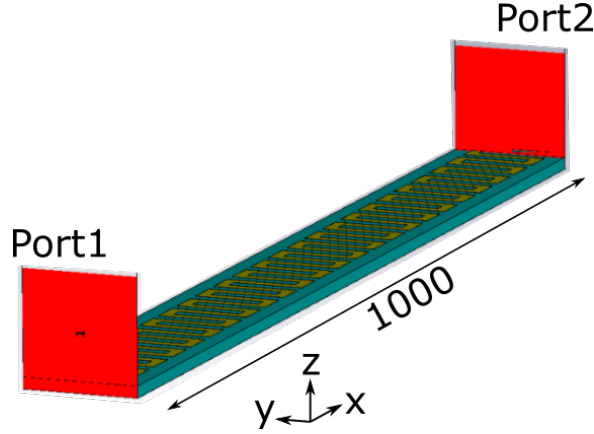
Figure4.3: Simulation model of zigzag pattern. The $\pm y$ boundary conditions are the magnet wall. Various w_{zig} and thickness are simulated to estimate the maximum efficiency.

Table4.1: Sheet Parameter

Symbol	Value	Unit	Description
ϵ_S	$2.0\epsilon_0$	F/m	Dielectric constant of dielectric in sheet
μ_S	$1.0\mu_0$	H/m	Permeability of dielectric in sheet
ϵ_O	8.85×10^{-12}	F/m	Dielectric constant of air (outside space of sheet)
μ_O	1.26×10^{-6}	H/m	Permeability of air (space outside the sheet)
ω	$2\pi f$	rad/sec	Angular frequency of EM wave
L_{cp}	1	m	Length of coupler
d_{cp}	100	m	Transmission distance
$\tan\delta$	0.0005		Loss tangent
ρ_S	2.82×10^{-8}	$\Omega \cdot m$	electrical resistivity

w_{zig} and the thickness were varied, and efficiency for each frequency in each parameter was obtained. The other sheet parameters are shown in Table 4.1.

Fig. 4.4 shows the efficiency when varying w_{zig} with a constant thickness. The thickness is 10-mm. At 13.56 MHz, the efficiency decreases as w_{zig} increase. This is because the influence of the propagation loss is strongly received as the alpha increases. Also, the frequency at which the efficiency peaks decreases. The optimum frequency can be reduced to around 1 MHz.

Fig. 4.5 shows the efficiency when the thickness is varied with 60-mm w_{zig}. As the thickness decreases, the propagation loss cannot be ignored and the efficiency decreases. A thickness of 10-mm is required to extend the distance to 100-m using 13.56 MHz. When w_{zig} is 60-mm and thickness is 10-mm, the efficiency becomes the maximum at 13.56 MHz.
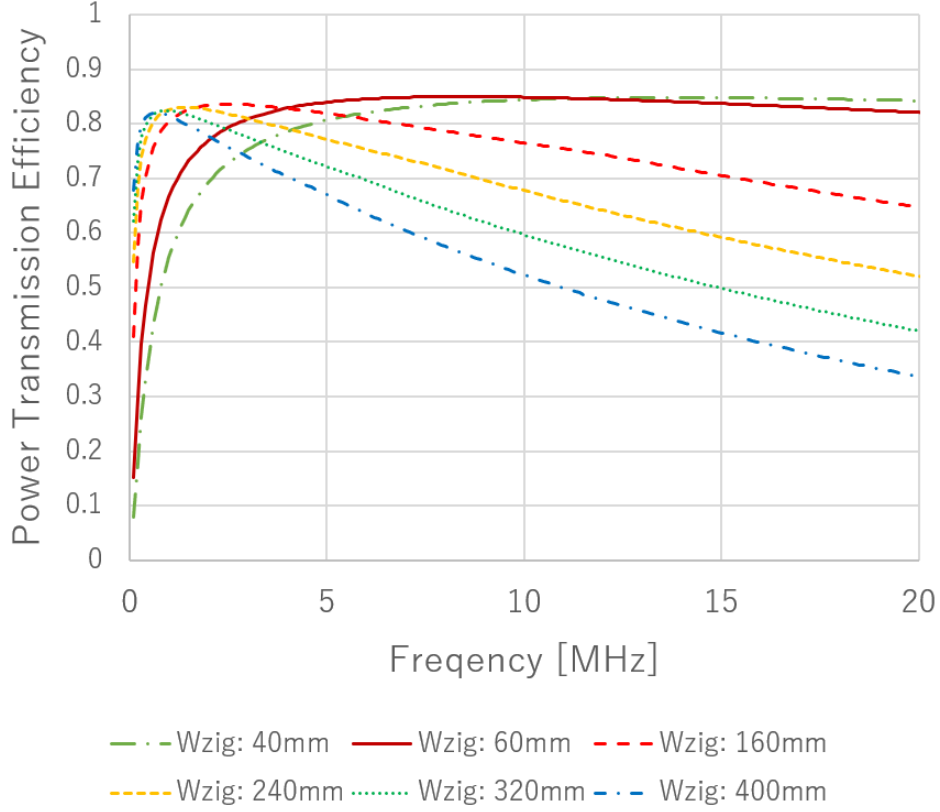
Figure4.4: Efficiency when varying w_{zig} with 10-mm thickness.

4.2.1   Sheet characteristics summary

The sheet characteristics are summarized in Table. 4.2. The 84% maximum efficiency satisfies the target value.

4.2.2   EM power leakage ratio

In order to evaluate the safety of the sheet having the parameters of Tables. 4.1 and 4.2, the power leakage ratio was calculated. The power leakage ratio is defined by the following equation [7].

$$r_{leak} = \frac{\omega \epsilon_0}{2} \left(\frac{\gamma}{1+\gamma} \right)^{3/2} \sqrt{X_0/B_S}, \tag{4.2}$$
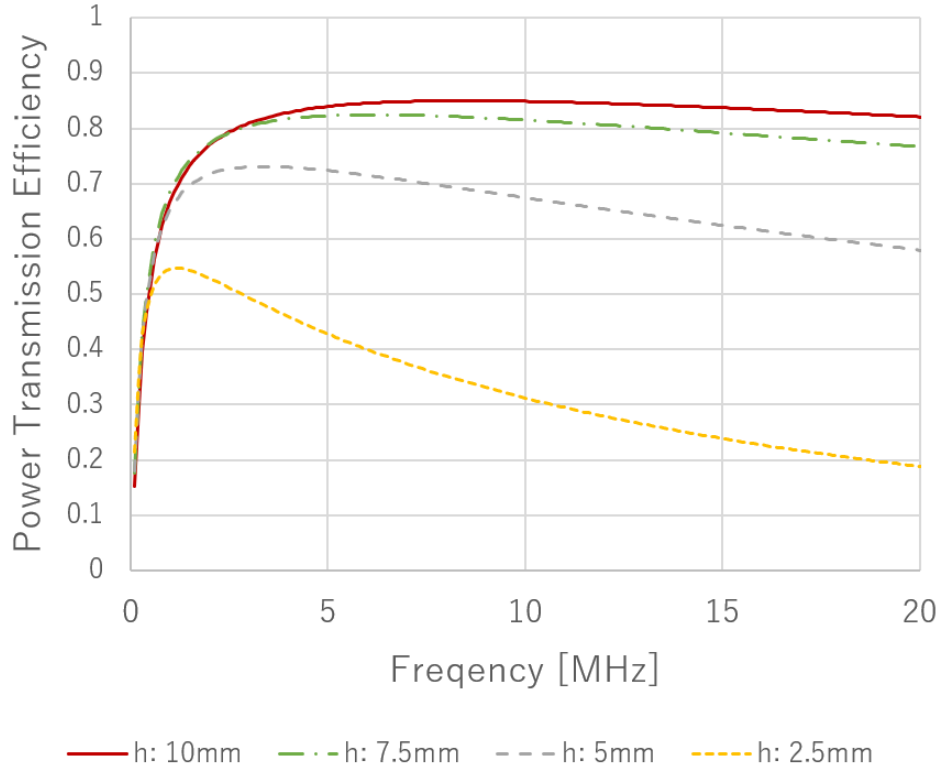
where

Figure4.5: Efficiency when varying thickness with 60-mm w_{zig}.

Table4.2: Sheet Characteristics

| Symbol	Value	Unit	Description
w_{zig}	60	mm	Surface resistance
p_{zig}	20	mm	Surface resistance
h	10	mm	Sheet thickness
R_0	0.004798	Ω/m^2	Surface resistance
X_0	5.7	Ω/m^2	Surface reactance
Q_0	1585		Dielectric constant of air (outside space of sheet)
R_{sx}	6.67	$\Omega \cdot m$	Characteristics impedance
α	0.000364		Attenuation constant
f	13.56	MHz	Operating frequency
η	84	%	Estimated maximum efficiency
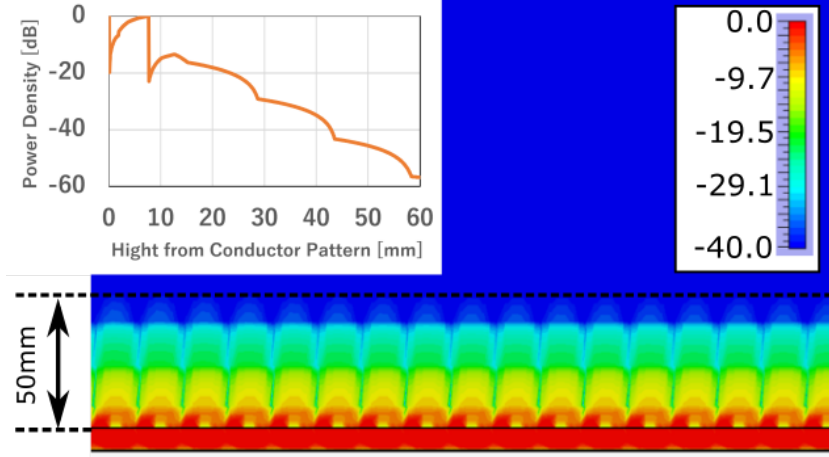
Figure4.6: Power density in the xz-plane of the simulation model.

$$\gamma \equiv \frac{X_0 B_S}{(\mu_S \epsilon_S - \mu_0 \epsilon_0)\omega^2} \tag{4.3}$$

$$B_S \equiv \omega \frac{\epsilon_S}{h} \tag{4.4}$$

$$\tag{4.5}$$

The leakage ratio is determined by the sheet reactance. On the other hand, too large a reactance increases propagation loss. For this reason, distance constraints and safety constraints are not contradictory factors.

The calculated power leakage ratio is 0.3%. And the simulated result of the power density is shown in Fig. 4.6. The highest power density in the sheet is set to 0 dB. The power density attenuates to -40 dB above 50-mm from the surface.

4.3 Conclusion

This chapter presented high-inductive surface pattern that realizes sufficient reactance at 13.56 MHz ISM band. Based on the equation for calculating the efficiency, the optimum sheet parameter was determined. As a result, the feasibility of the long distance WPT system was shown. The estimated maximum efficiency is 84%, which exceeds the target value.

Actually, the receiving coupler and the impedance matching circuit are not mentioned in this chapter. In order to realize the maximum efficiency shown in this chapter, a low loss of receiving coupler is required.

Part II

Energy-Efficient Wireless Communication and Battery-Less Body Sensor Network Using Sheet-like Medium

Chapter 5

Low Power and High Speed Data Transmission System

5.1   Indoor Wireless Sensor Networks

5.1.1   Low power communication systems

A developing CMOS technology and an increasing variety of low power communication systems enable battery-driven sensor nodes in wireless sensor networks (WSNs) and the Internet of Things (IoT). ZigBee and Bluetooth are representative wireless communication standards used in battery-driven WSN. On the other hand, their energy-per-bit rate (EBR), which is the energy required per a single bit transfer, is higher than that of conventional Wi-Fi [21]. EBR determines the maximum amount of information that can be transferred within their battery life. For example, a ZigBee device driven by an AA-sized battery, in which roughly 10,000 J of energy is stored, can transmit at most 1 GB of information [22].

In other words, the EBR and the battery capacity determine the battery life. Suppose a temperature sensing application that operates at 10-Hz sampling-rate with the 10-bit resolution of digital to analog converter (DAC). Its data rate, 100 bps, enables 28,000-hours operation of ZigBee transmitter with a 10,000-J AA-battery. A sound sensor, operating at 40-kHz sampling-rate and 10-bit DAC, generates 400-kbps data stream. In this case, the battery life is reduced to only 7 hours. To extend the battery life, the EBR has to be reduced.

At the expense of very short communication range up to a few centimeters, Transfer-Jet [23] can operate at 2–3 orders of magnitude lower EBR than ZigBee. Although its remarkably high energy efficiency is attractive, its very short transmission range is not acceptable in room-scale WSNs. Two-dimensional communication (2DC) can expand the range of TransferJet.
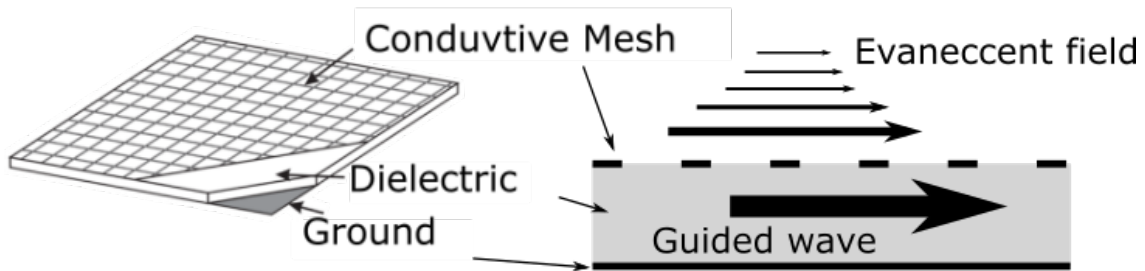
Figure5.1: 2DC sheet.

5.1.2 Two-dimensional communication sheet

2DC is a short-range communication scheme using a sheet-like waveguide shown in Fig. 5.1 [7]. The 2DC sheet guides electromagnetic waves and generates evanescent (non-radiative) field above its surface. It enables low emission and wide frequency range communication between transceivers laid on the sheet surface. The system can be constructed as "an extremely low power radio station (ELPRS)", which is defined as a radio station that generates an electric field intensity less than 35 /m at 3 m distant from the radio equipment [24]. While the requirement on the intensity of the radiated electromagnetic field is satisfied, the frequency range that an ELPRS occupies is not restricted.

5.1.3 2DC tile system

A 2DC tile system is shown in Fig. 5.2. Two-dimensional area (floor) can be covered with multiple parallel 1-D chains or with a long meander chain of 2DC tiles [25]. To keep the available signal power almost constant across the entire tile system, an amplifier is embedded in each base layer and compensates the signal loss.

Each waveguide sheet is electromagnetically isolated from the other sheets, i.e., the guided modes of them do not interact with each other. This means that the transmitted signal reverberates inside the 50-cm square waveguide sheet. The reverberation in such a lossy small area results in a small delay spread about 8–10 ns [26]. The delay spread of ordinary indoor wireless communication, where radio signals reverberate in a room-scale three-dimensional space, is 100-150 ns on an average and generally varies an order of magnitude due to scattering and absorption by objects/people in the environment. The symbol rate of ZigBee and Bluetooth is less than 1 Mbps. Its symbol duration is greater than 1 s which is 7–10 times longer than the average delay spread. On the other hands, since the signal propagation paths in tiles are electromagnetically almost isolated from the outside space, the delay spread is little affected by objects/people in the room.
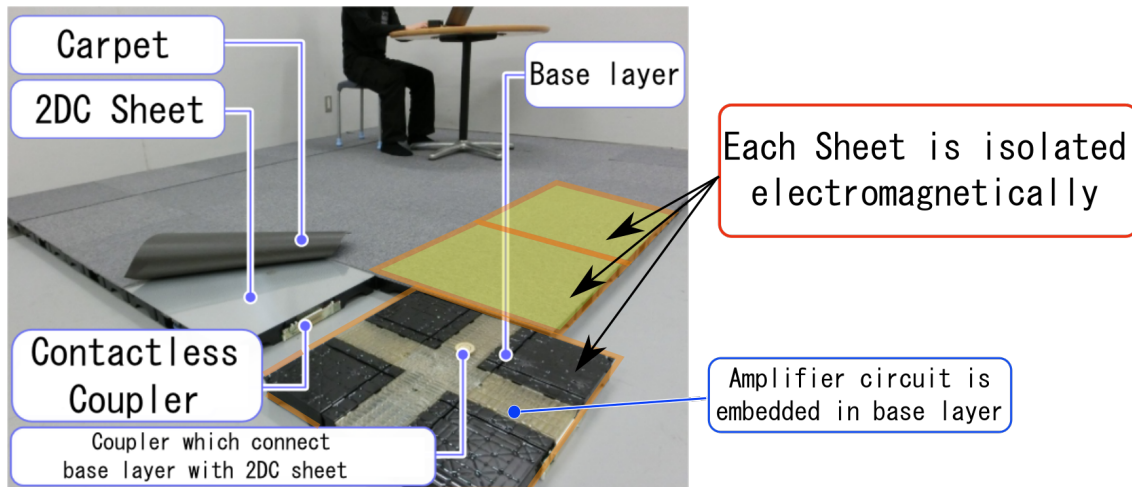
Figure5.2: 2DC tile system installed on the floor of a room.

5.1.4   A low power and high speed data transmission system based on 2DC

To figure out the motivation of high-speed and low power transmission in the 2DC environment, related technologies are compared in Fig. 5.3, in terms of the energy-per-bit rate (EBR), which is the ratio of the power consumption to the transmission rate, transmission rate, and communication range. Those data are based on evaluation of commercially available modules [23][27]. Related technologies mapped in the figure are: ZigBee, Bluetooth, WiFi (IEEE 802.11b), Passive Wi-Fi [27] and TransferJet [23]. The experimental result shown in 5.2.2 is also shown as the specification of 2DC.

Fig. 5.3 shows that transmission system based on 2DC technology can reduce EBR by reducing the power consumption of analog radio frequency (RF) components as well as TransferJet and Passive Wi-Fi, while achieving a room-scale communication range.

The major factors of power consumption are classified into the following two components: the analog RF component to generate RF signal transmitted from the antenna and the digital component to process baseband signals. The EBR can be drastically reduced as the analog RF power consumption is reduced. As the evidence, the EBR of TransferJet and Passive Wi-Fi are at least 1–2 orders of magnitude lower than other schemes in the dashed box shown in Fig. 5.3.

By connecting 2DC tiles side by side, the communication range is extended to a room-scale.

2DC tile system enables signal transmission/reception by all the devices laid on the floor, and even on any furniture covered with 2DC sheets. The devices can communicate with the low emission power density of −41.3 dBm/MHz [28]. This is significantly lower than the antenna power of conventional ZigBee devices, which is 0−+20 dBm in 2-MHz channel bandwidth. Hence, the EBR can be reduced in 2DC.
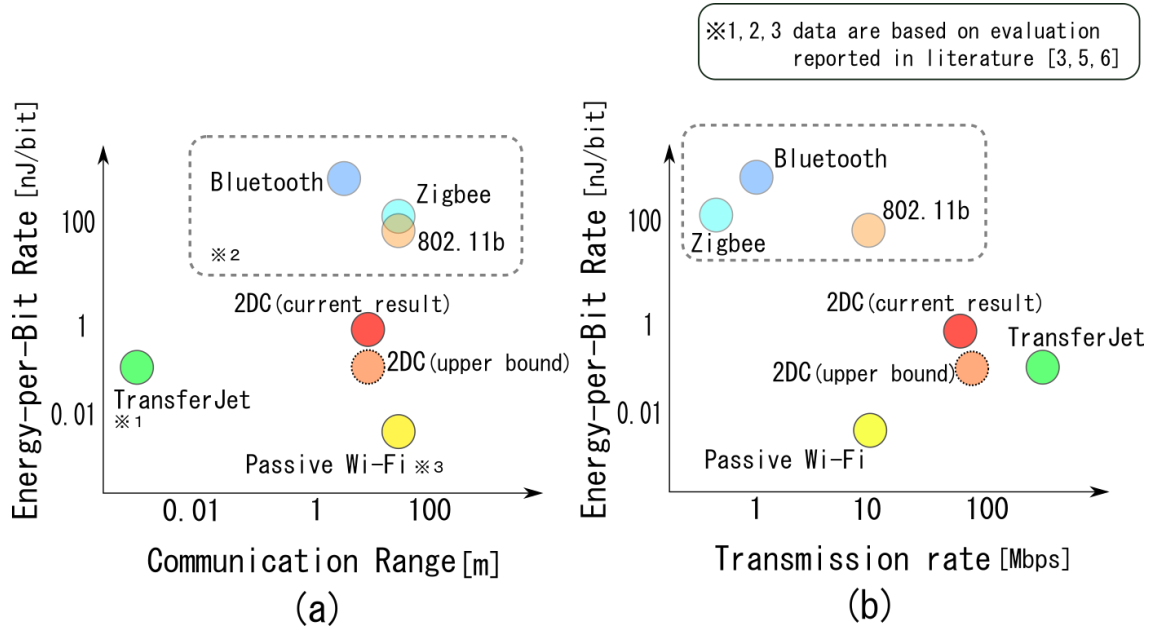
Figure5.3: Evaluation of representative communication standards in terms of (a) EBR versus communication-range, and (b) EBR versus transmission-rate.

5.2   Preliminary Experiment of Energy Efficient Signal Transmission

In this section, we report on a preliminary experiment of energy efficient signal transmission using TransferJet devices on a two-dimensional communication (2DC) system, as a feasibility study of a low-EBR room-scale communication system. It achieved a data rate higher than 70 Mbps with an EBR of 1.7 nJ/bit on a 50-cm square 2DC sheet. The EBR is significantly lower than that of ZigBee. We also explain the feasibility of a room-scale communication system at a higher data rate with such a low EBR of the mobile nodes based on 2DC technology.

5.2.1   Concept of energy-efficient signal transmission on 2DC

While the symbol duration is longer than the average delay spread, signal can be transferred with acceptable inter-symbol interference (ISI). Thus, the devices can transmit signal at high symbol rate, which enables high data transmission rate with a single or a few carriers. The digital logic component of single-carrier transceivers can be much simplified compared with a modulation circuit for orthogonal frequency-division multiplexing (OFDM) [29].

To avoid significant ISI, the symbol duration should generally be about 10 times greater than the delay spread of a channel. In a waveguide sheet with an 8–10-ns delay spread, a

100-ns symbol duration signal, which corresponds to 10-MHz symbol rate, can be transferred without significant ISI. Assuming complementary code keying (CCK) with 8 bit per symbol, 80 Mbps will be enabled.

As a result, the transceiver which optimizes the symbol rate for room-scale 2DC environments can communicate with low emission power density of -41.3 dBm/MHz while providing 80 Mbps transmission rate. Its communication range is at most 17 meter.

5.2.2   Experimental results

In this subsection, we present experiments to demonstrate the feasibility of low emission and high transmission rate 2DC. We measured the transmission rate of a single-carrier high-symbol-rate 2DC system, by using a commercially available TransfeJet adapter, SANWA SUPPLY ADR-TJMUBK.

TransferJet is one of extremely low power radio stations (ELPRSs). Its symbol rate of 280 MHz, which corresponds to a symbol duration of 3.57 ns, will undergo significant ISI in a 50-cm square sheet.

Fig. 5.4(a) shows the measurement environment. One of two TransferJet adapters, attached to a PC, was connected to the feeding point of 2DC sheet with a coaxial cable. The other one, attached to another tablet PC, is connected to a proximity coupler laid on the sheet. To connect the coaxial cables, an SMA connector was soldered on each TransferJet circuit board.

We measured the transmission rate at three different coupler positions. The delay spread of the 2DC channel, from the feeding point fixed on a sheet edge to the proximity coupler, depends on the coupler position, because a standing wave is generated due to the open-edges of the sheet [26]. The delay spread was measured with a vector network analyzer (VNA) at each coupler position. While keeping the coupler position unchanged, VNA ports were connected to the feeding point and the coupler, instead of the TransferJet devices. VNA measured a scattering parameter (S-parameter) from the feeding point to the coupler in the frequency domain. It was converted into the time-domain impulse response by the inverse Fourier transform [26].

5.2.3   Discussion about experimental results

The three measurement results are shown in the transmission-rate versus delay-spread plot, Fig. 5.4(b). The EBR also shown in the same graph was calculated from its transmission rate and power consumption of 118 mW, that was published in [22]. At a coupler position where the delay spread was 3.9 ns, the transmission rate achieved 71.1 Mbps and the corresponding EBR was 1.7 nJ/bit. This result is also plotted in Fig. 5.3. The transmission rate slower than the original TransferJet is due to the bit error more frequently caused by a significant ISI. By optimizing the symbol duration, the transmission rate will
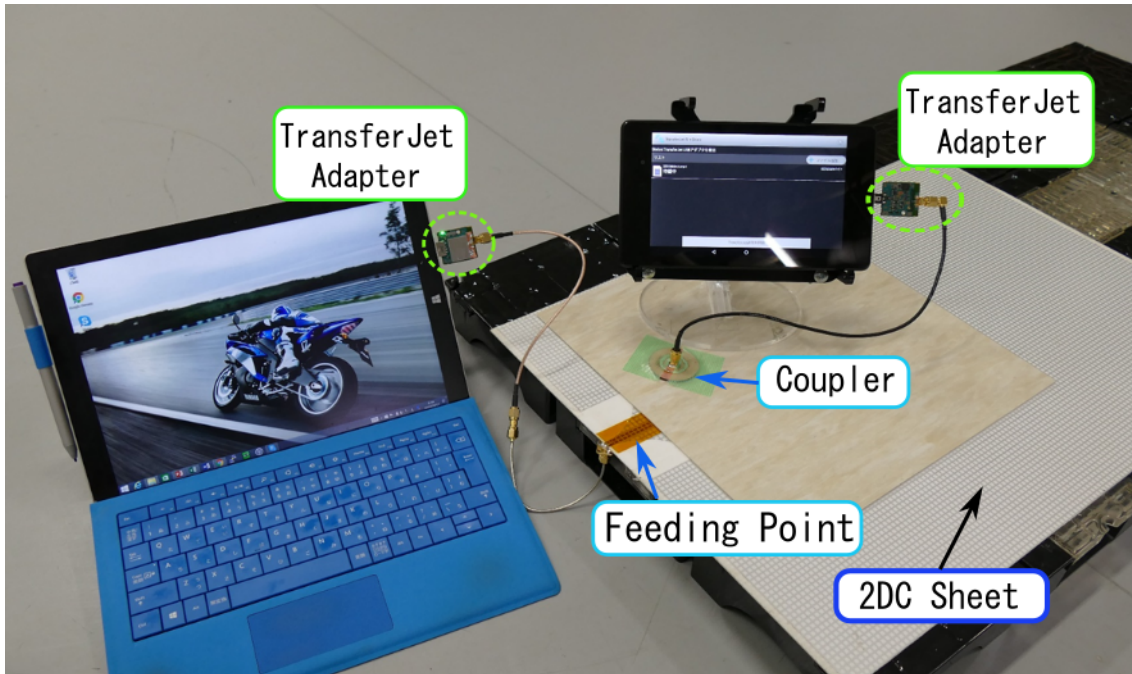
(a)
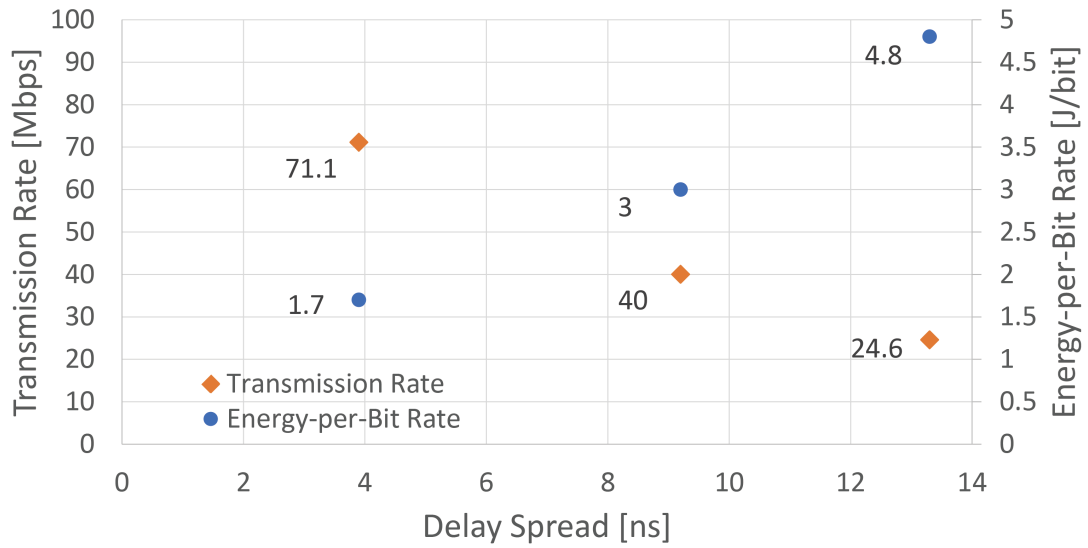
(b)

Figure5.4: Transmission rate and EBR were evaluated on a 2DC sheet by using a pair of TransferJet adapters. (a) The measurement environment and (b) measured results.

be maximized at any arbitrary coupler position on the entire 2DC area.

5.3   PHY Layer Design for Energy-Efficient Data Transmission

The ensuing subject of interest would be the theoretical limit of EBR for the optimal physical layer (PHY) parame-ters selected for a 2DC environment, considering the delay spread and signal-to-noise ratio (SNR) for a typical 2DC sheet. In this section, we present a method to determine the optimum PHY parameters to minimize the EBR. Using the determined parameters, the numerical simulation shows that a transmission rate of 36 Mbps is achieved with a power consumption of 24 mW. EBR is 0.66 nJ/bit. This transmission rate was supported by the experiments. These results present the feasibility of energy-efficient communication in 2DC.

5.3.1   Propagation in 2DC

As mentioned above, 2DC environment enables the use of UWB in the range of 3.1 to 10.6 GHz. Moreover, the influence of ISI is less than ordinary room-scale (50−150 m^2) OTA communication environment. The bit error caused by ISI is increased by increasing the ratio of root-mean-square (RMS) delay spread to symbol duration time S_{DT}. The RMS delay spread σ_τ of a 50-cm square sheet is approximately 8−10 ns whereas the RMS delay spread of room-scale OTA environment is approximately 100−150 ns [26]. Therefore, high-speed communication with high symbol rate S_R ($=1/S_{DT}$) can be realized in 2DC environments. Moreover, it can reduce the power consumption of a digital signal processor because it does not require the high calculation cost of secondary modulation loading such as orthogonal frequency-division multiplexing.

In general, the RMS delay spread is scaled up by in-creasing the size of the communication environment. However, the RMS delay spread of the 2DC tile system is not scaled up by increasing the number of tiles. The RMS delay spread is maintained at approximately 10 ns [26] since each tile is electromagnetically independent. Thus, high-speed low-radiation communication can be achieved even for terminals that are either several meters away from each other or on a single tile.

5.3.2   PHY design minimizing EBR

This section presents a method for determining PHY parameters that minimize EBR. Specifically, E_b and S_R, which minimize EBR, are determined by solving the trade-off problem between transmission data rate and power consumption. Further, E_b denotes the received energy per bit.

The EBR is expressed as follows.

$$R_{EBR} = \frac{W}{T} \tag{5.1}$$

where R_{EBR} denotes the value of EBR, W denotes the power consumption, and T denotes the transmission data rate.

In this thesis, the theoretical limit of transmission rate (channel capacity C) is evaluated based on the entropy [30] as

$$C = H(Y) - H(Y|X) \tag{5.2}$$

where X and Y denote the transmitted and received codes, respectively, and H(Y) denotes the information bits received from the information source per second. Thus, $H(Y)$ is expressed as follows.

$$H(Y) = kS_R, \tag{5.3}$$

where k denotes the value of bits per symbols. The lost entropy $H(Y X)$ in a communication path with the bit error rate (BER) expressed as follows.

$$H(Y|X) = kS_R(1-\rho)(-\log_2(1-\rho)) + \rho(-\log_2(\rho)), \tag{5.4}$$

Notably, C determines the upper bound of the number of bits that can be transmitted per second, which also includes the error correction code and the number of bits used for the frame. In this study, we focus on the effect of PHY parameters. The influence of an upper layer such as the media access control (MAC) layer is not considered here.

Subsequently, we describe the derivation of the BER. In general, there are some factors influencing BER. If the BER caused by independent factors is sufficiently smaller than 1, BER is obtained as their sum. Further ρ and ρ_{SN}, which is the BER caused by SNR, are defined as

$$\rho = \rho_{SN} + \rho_{ISI}, \tag{5.5}$$

where

$$\rho_{SN} = \frac{1}{2}\text{erfc}(\sqrt{k\frac{E_b}{N_0}}), \tag{5.6}$$

where ρ_{ISI} is the BER caused by ISI and N_0 donates the thermal noise power in a bandwidth of 1 Hz. Further, ρ_{SN} has different representation methods depending on the

modulation system. We assume binary phase-shift keying (BPSK) modulation in this study.

An equivalent transmission path (ETP) model [31] described a propagation environment by using two waves a leading wave and a delayed wave. A key parameter that determines ρ_{ISI} is the RMS delay spread σ_τ in the Rayleigh fading environment. The ETP model can significantly simplify the description of a propagation channel, while it conserves the essential parameter σ_τ.

The variable r is defined as the ratio of amplitude of the leading wave to that of the delayed wave. Further, ϕ is a phase difference between the leading wave and delayed wave. The delay time of the delayed wave is denoted as $\Delta\tau$. The value of ρ_{ISI} when the aforementioned variables assume a certain value is expressed as

$P_0\{r, \phi; \Delta\tau(\sigma_\tau)\}$ for $\sigma_\tau/S_{DT} < 0.5$ the probability density function of the aforementioned variables is expressed as

$$f_R\{r, \phi\} = \frac{1}{\pi} \frac{r}{(r^2+1)^2}, \tag{5.7}$$

where ϕ follows a uniform distribution in the Rayleigh fading. In general, assuming Rayleigh fading, f_R is independent of σ_τ.

We define $f'_R\{r; \sigma_\tau\}$ as follows.

$$f'_R\{r, \sigma_\tau\} = \int_0^2 \pi f_R\{r, \phi; \sigma_\tau\}d\phi = \frac{2r}{(r^2+1)^2}. \tag{5.8}$$

The variable $\Delta\tau$ is expressed as follows.

$$\Delta\tau = 2\sigma_\tau. \tag{5.9}$$

Further, ρ_{ISI} is obtained as the product of P_0 and f_R. Based on the above discussion, ρ_{ISI} is expressed as follows.

$$\rho_{ISI}(\sigma_\tau) = \int_0^\infty f'_R\{r; \sigma_\tau\}\left(\int_0^2 \pi P_0\{r, \phi, \Delta\tau(\sigma_\tau)\}d\phi\right)dr. \tag{5.10}$$

In (5.10), P_0 is obtained by using simulation software, which calculates the BER of a communication system. P_0 calculated in the r- ϕ plane is called the BER map [31]. BER map must be calculated according to each $\Delta\tau$, which differs for every σ_τ. An approximate equation by using only one BER map is proposed in [32] to decrease the calculation load in creating many BER maps. It uses the shape correlation between $\Delta\tau$ and the BER map.

Further, $P_0\{x, \phi; \Delta\tau_{map}\}$ denotes a BER map in the approximate equation of 5.9, $\Delta\tau_{map}$ denotes $\Delta\tau$ in a BER map, x is the logarithmic expression of r, and x and ϕ are discrete

values with the step widths of Δ_x and $\Delta\phi$, respectively. If $(\Delta\tau_{map})/S_DT$ <0.5, the value of $\Delta\tau_{map}$ can be set arbitrarily. Moreover, $(\Delta\tau_{map})/S_{DT}$ =0.2 is recommended [33] and we followed it. The range of x and ϕ is assumed until P_0 is sufficiently close to 0. We set the range of x from -7.5 to 7.5 with Δx=0.25. Furthermore, the range of ϕ is set from 90 to 270 with $\Delta\phi$ Based on the above discussion, ρ_{ISI} is expressed as follows.

$$\rho_{ISI}(\sigma_\tau) \approx \eta^2 \Delta x \Delta\phi \sum_x g_R(\eta x) \left(\sum_\phi P_0\{x, \phi; \Delta\tau_{map}\} \right), \tag{5.11}$$

$$\eta = \frac{2\sigma_\tau}{\Delta\tau_{map}}, \tag{5.12}$$

$$g_R(\eta x) = \frac{1}{b}\exp\left(\frac{x}{b}\right) f_R'\left\{\exp\left(\frac{x}{b}\right); \sigma_\tau\right\}, \tag{5.13}$$

$$\tag{5.14}$$

where

$$b \equiv 20\log_{10} e. \tag{5.15}$$

The power consumption is the sum of the RF component W_{RF} and digital component W_{DSP} expressed as follows.

$$W = W_{RF} + W_{DSP} \tag{5.16}$$

Further, W_{RF} of the transmitter is defined as

$$W_{RF} = \frac{kS_RE_b}{L_b}, \tag{5.17}$$

where L_B is the propagation loss between the transmitter and receiver. It is the ratio of the received signal power to the transmitted signal power.

While UWB enables the use of wideband, its restriction on power density is -41.3 dBm/MHz, which is less than one ten thousandth that of Wi-Fi. Thus, spread spectrum is necessary to ensure SNR. The bandwidth diffused by pseudorandom noise (PN) code is equal to the chip rate C_R, which is the clock frequency of the PN code. W_{DSP} is proportionate to the clock frequency of a circuit [34].

The clock frequency of a circuit should be low to reduce W_{DSP}. However, in order to realize a desired chip rate, a proportionate clock frequency is necessary. W_{DSP}, which is proportional to C_R, is expressed as follows.

$$W_{DSP} = \alpha C_R, \tag{5.18}$$

where α denotes a constant of proportionality determined by the characteristics of the circuit.
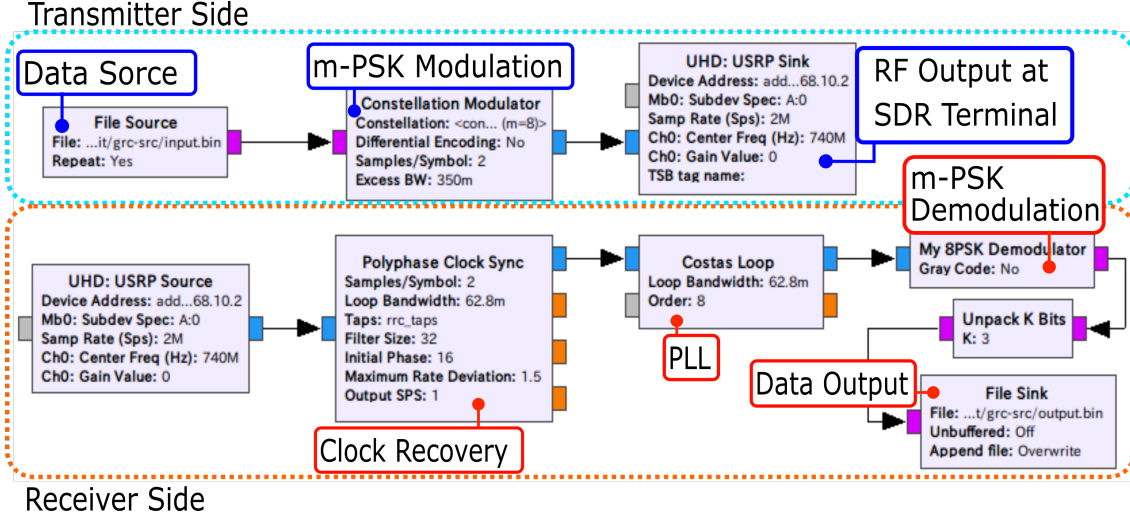
Figure5.5: Flow diagram of prototype system in GNU Radio.

5.3.3   Prototype Communication System

A prototype communication system is created by using GNU Radio [35], which is the development environment of software-defined radio (SDR). The flow diagram of a prototype system in GNU Radio is shown in Fig. 5.5. Moreover, the specifications of this system are given in Table 5.1. A 50-cm square 2DC tile is assumed as the communication environment. Owing to the multi-reflection at the edge of the waveguide sheet, a standing wave is generated. Thus, the attenuation from the transmitter to receiver is dependent on the position. In this study, we adopted -30 dB as its representative value.

A digital signal processing method of prototype system resembles that of the TransferJet system. These systems realize high-speed communication at a high symbol rate with single carrier without requiring the high calculation cost of secondary modulation loading. Thus, the value of α is determined from the data sheet of TransferJet [23]. Notably, the prototype does not equalize the received signal to measure ρ_{ISI} without a digital correction.

### 5.3.4   Calculated Result and Evaluation

This subsection aims to calculate EBR at each value of E_b/N_0 and σ_τ/S_{DT} based on the prototype communication system mentioned in the above subsection and the equations mentioned in Section 5.3.2. A trade-off will be described with the calculation results.

The calculated values of R_{EBR} at each value of E_b/N_0 and σ_τ/S_{DT} are shown in Fig. 5.6. It shows two trade-off factors: one between ρ_{ISI} and the transmission rate determined by S_R $(=1/S_{DT}$ $)$ and the other between ρ_{SN} and W_{RF}.

In Fig. 5.6, the relationship between σ_τ/S_{DT} and R_{EBR} at E_b/N_0 $=14$ demonstrates the first trade-off. The transmission rate increases by increasing S_R. Thus, R_{EBR} decreases

Table5.1: Specifications of prototype system

The parameters of communication environment	
σ_τ	10 ns
L_B	$1\ 10^{-3}$
N_0	-174 dBm/MHz
The parameter of communication system	
k	1
C_R	50 MHz
α	$3.6\ 10^{-10}$ J/Hz
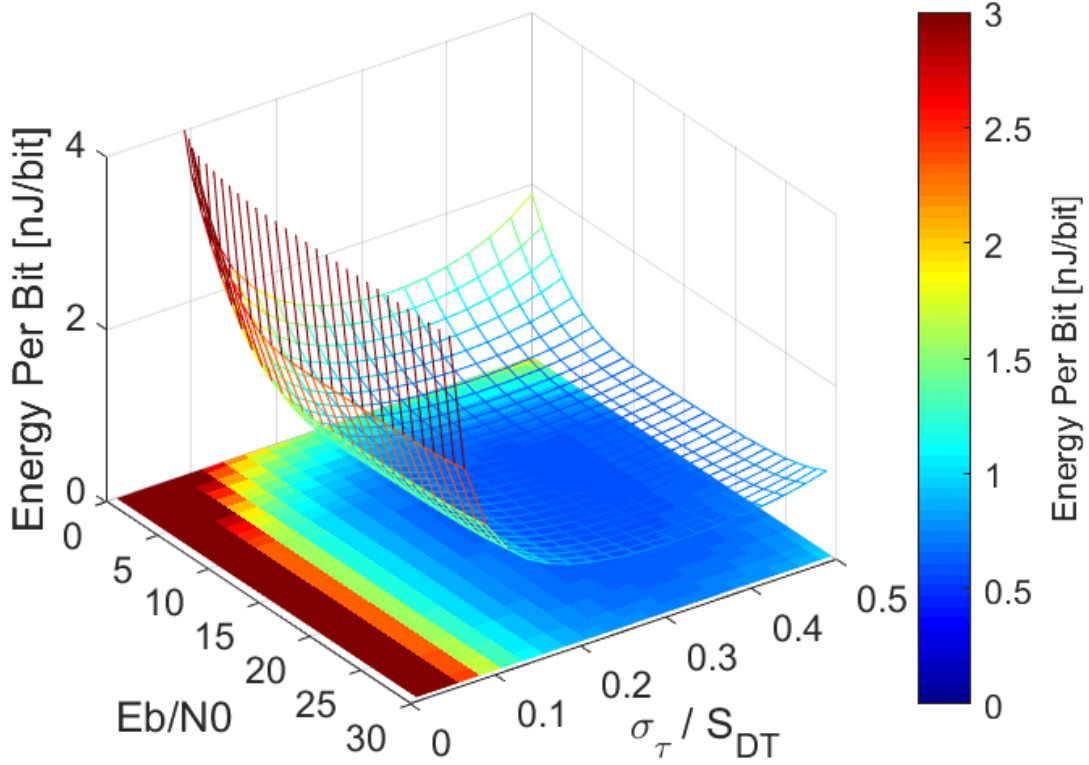
Figure5.6: Calculated values of R_{EBR} at each value of E_b/N_0 and σ_τ/S_{DT}.

until σ_τ/S_{DT} =0.35. However, R_{EBR} starts to increase at σ_τ/S_{DT} =0.35 because ρ_{ISI} and W_{RF} increase in S_R.

The relationship between E_b/N_0 and R_{EBR} at σ_τ/S_{DT} =0.35 demonstrates the second trade-off. The transmission rate increases by increasing E_b. Further, ρ_{ISI} becomes lower than 10^{-8} at E_b/N_0 =14. R_{EBR} starts to increase at E_b/N_0 =14 because W_{RF} increases in E_b.
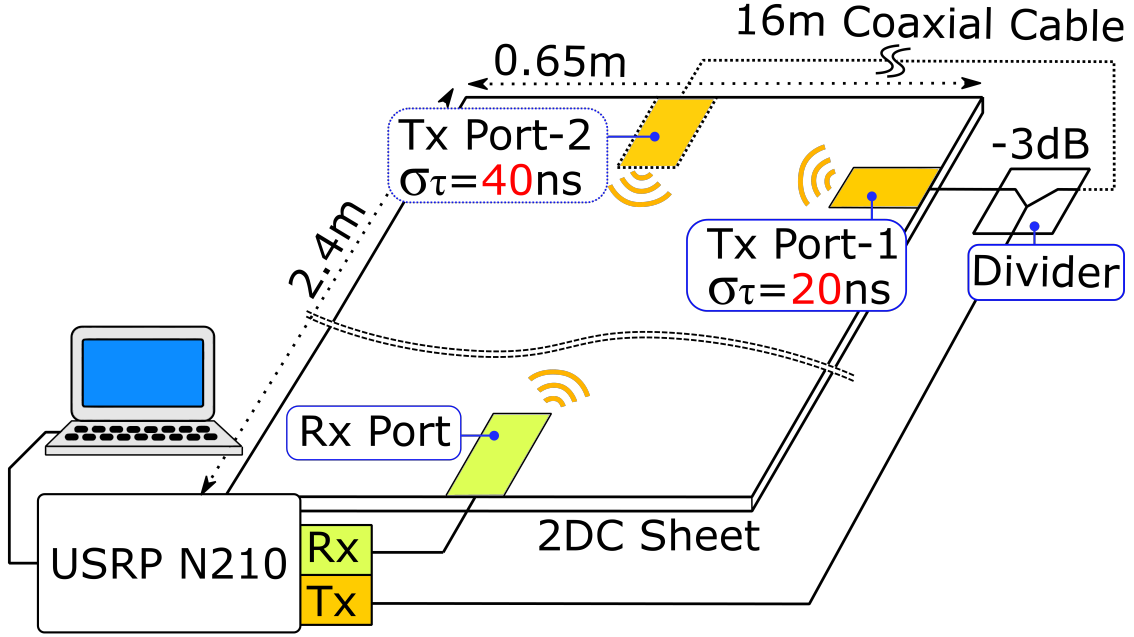
Figure5.7: Experimental setup.

The power consumption is 24 mW and the transmission rate is 36 Mbps. These values are calculated using E_b and S_R when R_{EBR} is minimized in Fig. 5.6. EBR is 0.66 nJ/bit. Moreover, the transmission rate in this study does not consider the influence of the layer above the PHY. Thus, the actual transmission rate will be lower than the calculated results. However, even if the actual transmission rate is assumed to be half of the calculated value, the EBR is lower than the result reported in [36]. This indicates the usefulness of the proposed optimum PHY parameter detection method.

5.4   Experiment

This section presents the validity of the theoretical equations shown in section 5.3.1. In particular, we experimentally confirm the relationship between σ_τ/S_{DT} and ρ_{ISI}. The transmission rate is calculated based on ρ_{ISI}. The experimental result presents the feasibility of energy-efficient data transmission in 2DC environments.

5.4.1   Experimental setup

We measured ρ_{ISI} for each value of SR in two different experimental setups of σ_τ (=20,40 ns) as shown in Fig. 5.7. Notably, the experimental setup is distinct from the actual usage case since proximity coupling is not used.

A prototype communication system with the function shown in Fig. 5.5 is implemented by using SDR terminal (Ettus Research, USRP N210) and GNU Radio. However, in the m-PSK modulation/demodulation shown in Fig. 5.5, 8-PSK is used in this experiment

whereas BPSK is assumed in the Section 5.3.2. The acceptable error vector magnitude of BPSK is the largest in m-PSK. Further, ρ_{ISI} of BPSK does not change significantly in the range of measurable SR whereas 8-PSK changes drastically. Thus, 8-PSK is suitable to confirm the validity of the theoretical equations.

In the setup where ρ_{ISI} is 20 ns, one of the ports of the divider is connected to the Tx-Port1. The other one is terminated whereas it is connected to the Tx-Port2 through a 16 m coaxial cable when ρ_{ISI} is 40 ns.

In the experiment, an 8 MB data file was transferred from Tx-Port to Rx-Port of USRP. The BER was calculated based on the transmitted/received data. The BER is determined from the average of BER obtained at each window of window function processing.

Accordingly, 6,400 BER values were obtained from 8 MB (64 Mbit) transmitted/received data files by using the window function (window and step length were 10,000 bits). The average of 6,400 BERs is defined as ρ_{ISI} at each S_R. Note that this experiment aims to measure ρ_{ISI}. The transmitted signal power density was sufficiently large to reduce ρ_{SN}.

5.4.2   Experimental results

The experimental results are shown in Fig. 5.8. The increase in transmission rate slows down after S_R of 7 MHz when the RMS delay spread is 20 ns. The transmission rate starts to decrease at S_R of 6 MHz when the RMS delay spread is 40 ns. These experimental results and calculated results are generally consistent with each other. This indicates that high-speed communication with high S_R is feasible in a 2DC tile environment that has an RMS delay spread of 8–10 ns.

Assuming that E_b/N_0 is 15 dB, σ_τ is 40 ns, k is 3, and the other parameters follow Table 5.1, the power consumption W when S_R is 6 MHz can be calculated as 21 mW from 5.16, 5.17, and 5.18. EBR is 1.17 nJ/bit. It is higher than the simulated result (0.66 nJ/bit) obtained in Section 5.3.4 and lower than the result (1.7 nJ/bit) obtained in the previous work.

5.5   Conclusion

This chapter presented the technical outline of the room size 2DC and the proximity connector for easily connecting each tile. Next, the propagation model in the room size 2DC was shown, and the feasibility of high-speed and power-saving wireless communication was shown. By utilizing the communication environment that can ensure SN ratio that can communicate even with weak radio waves and has lower RMS delay spread than space communication, it is possible to perform wireless communication more than 100 times higher efficiency than general indoor wireless communication Become.
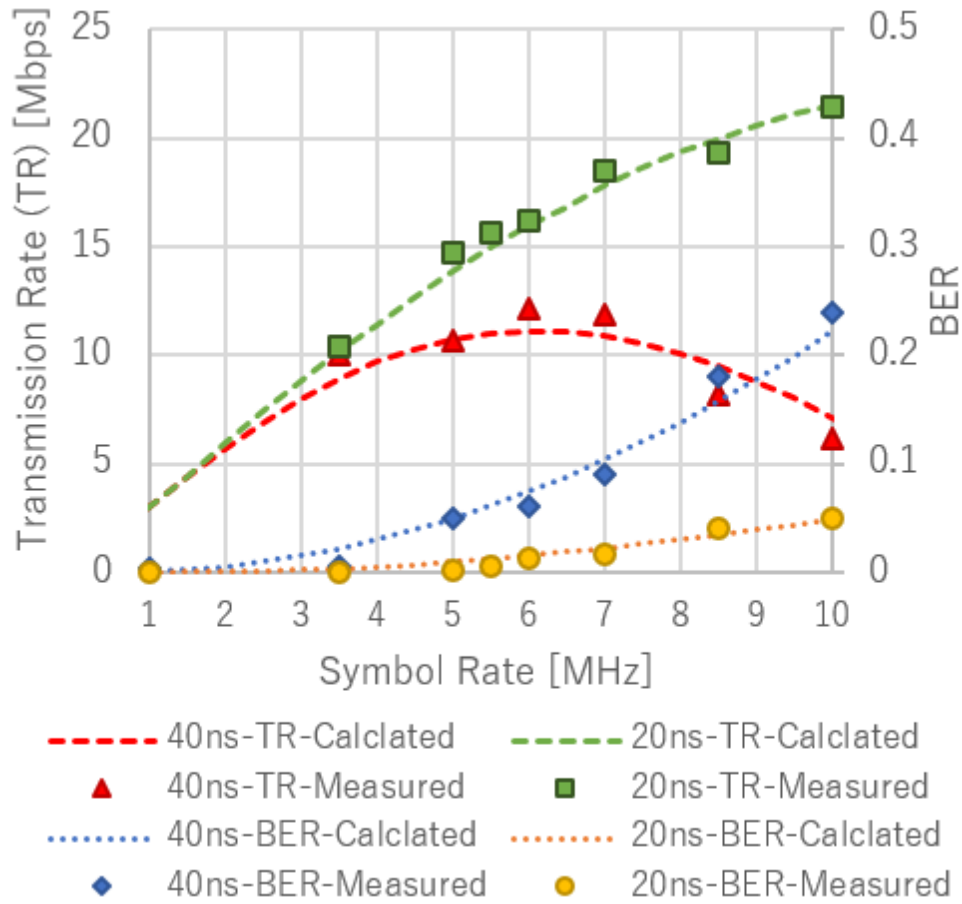
Figure5.8: Experimental result.

After confirming feasibility with commercially available weak wireless terminals, we proposed a method for determining optimal physical layer parameters. We actually implemented the communication protocol at the software terminal and carried out the experiment. In the experiment, the same result as the simulation result was obtained.

Chapter 6

Battery-Less Body Sensor Networks

6.1 Body Sensor Networks

Body Sensor Networks (BSNs) [37], which gathers data from worn sensor nodes to a host device, is a promising technology for health care [38], fitness [39], and so on. Popular BSN sensor devices are mostly watches, glasses, accessory types. A clothing type device has a function not found in accessories type devices such as acquiring biological information of the whole body.

One-to-one wiring to sensor devices on clothes are at high risk of wire breakage. When battery-driven wireless devices are distributed and arranged on clothes, battery replacement of each device impairs practicality. A two-dimensional transmission path called CTEF enables to wired connection with each device distributed on the clothing without one-to-one wiring.

6.1.1 Conductive-thread-embroidered fabric: CTEF

Fig. 6.1 shows the structure of the CTEF and tack-type connector [40][41]. The CTEF shown in Fig. 6.1 (a) is a transmission path, with a two-dimensional spread by sewing conductive threads on both sides of a cloth-like insulator. Fig. 6.1 (b) shows the cross-sectional view when a needle is pierced from the front side of the CTEF and fixed with a metallic clutch on the back side. In the tack-type connector, a metallic needle is fixed and conducted by soldering it to the surface of the double-sided copper clad board (the upper side of Fig. 6.1 (b)). The conductive threads on the front and back sides conduct with the backside of the board and the front side of the clutch when penetrating and fixing. If the backside conductive thread is grounded, the board surface can be designed as a ground.

It should be noted that the front-side conductive thread should not be in contact with the needle in order to prevent short circuit. The copper pattern on the bottom side of the board is also electrically isolated from the needle.
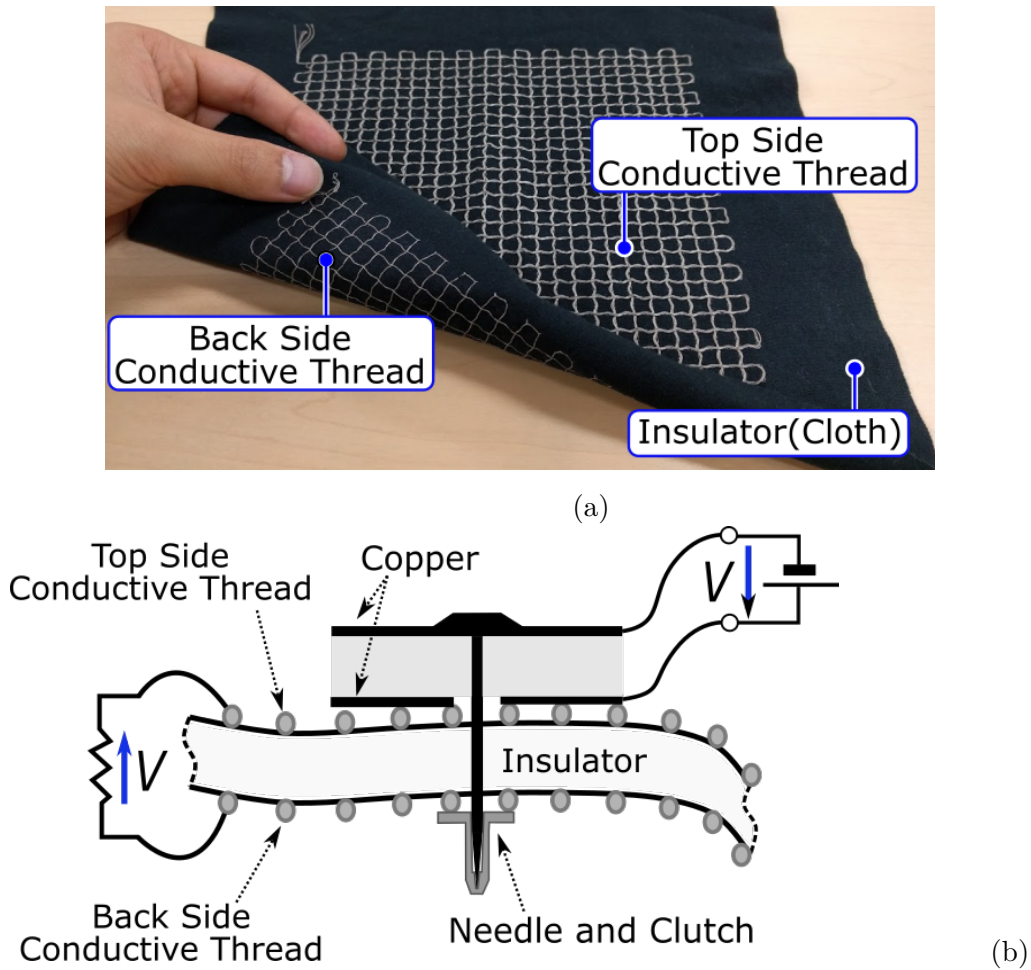
Figure6.1: (a) A conductive-thread-embroidered fabric. (b) Cross-sectional view when a tack connector is penetrated and fixed to a sheet.

6.1.2   BSN powerd by multiple power generation element

Energy Harvesting (EH) is a promising technology for wearable and Internet-of-Things (IoT) devices [42] [43] [44]. One power generation element in one device is common in conventional EH systems, while the use of multiple elements is rare [45]. While the sensor chip shown in Fig. 6.2 can be driven by one power generation element (PGE), the host device that collects data frequently from sensors cannot be, because it consumes significantly more power than one sensor chip. The energy generated in a small area/volume of the host device from its surrounding environment is insufficient to drive it. However, the host device may be driven by the entire body's energy, collected from multiple PGEs distributed across the clothing. However, the wiring to each PGE raises an implementation problem.
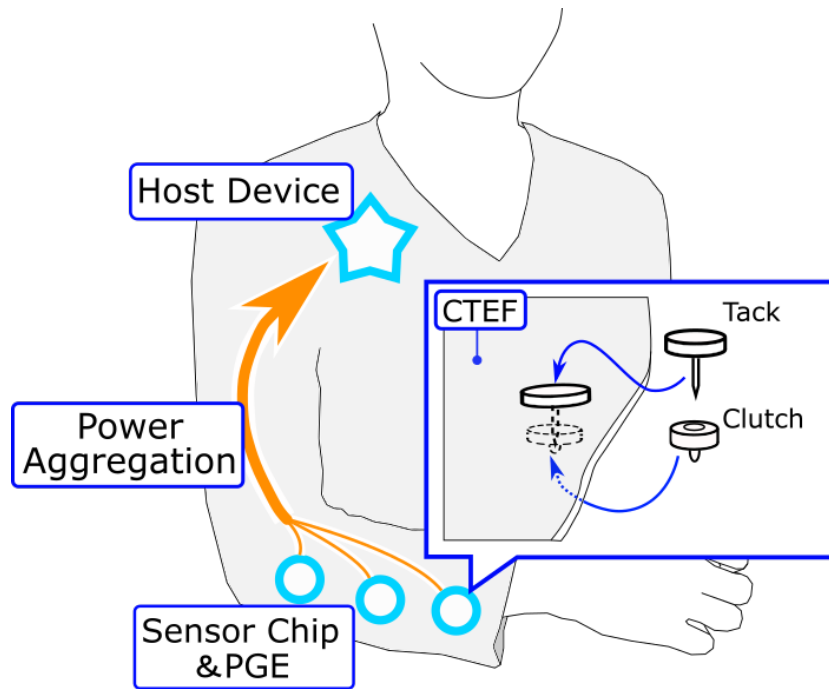
Figure6.2: Concept of power aggregation system by using wearable two-dimensional communication sheet and tack connector.

6.1.3 BSN powerd by NFC-coupled smartphone in the pocket

A batteryless sensor node can reduce the burden on the wearer because there is no trouble of charging and replacing batteries.

A wired BSNs can eliminate the battery of the sensor nodes. The CTEF can construct it without one-to-one wiring. In the wired connection BSNs, the sensor nodes can transmit/receive the data/power to/from a host device [40][41]. However, the host device still needs batteries for multiple sensor nodes and the host device itself.

We propose a batteryless host device. The proposed host device can transmit/receive the data/power to/from a smartphone in the pocket via a Near-Field-Communication (NFC) [46]. Fig. 6.3 shows the overview of the proposed batteryless BSNs.

In Fig. 6.3 , multiple batteryless sensor nodes are connected to the CTEF via a pin & socket connector without one-to-one wiring. The same is true for a batteryless host device connected in the pocket. The power source of the host device and the sensor nodes is obtained by harvesting the NFC radio waves emitted from a smartphone in the pocket.

NFC can remove the battery of the host device. The power consumption of an NFC transponder is about 10 mW [47]. Energy harvesting (EH) using NFC radio waves (NFC-EH) can acquire 40-50 mW as experimentally demonstrated in 6.3.2.
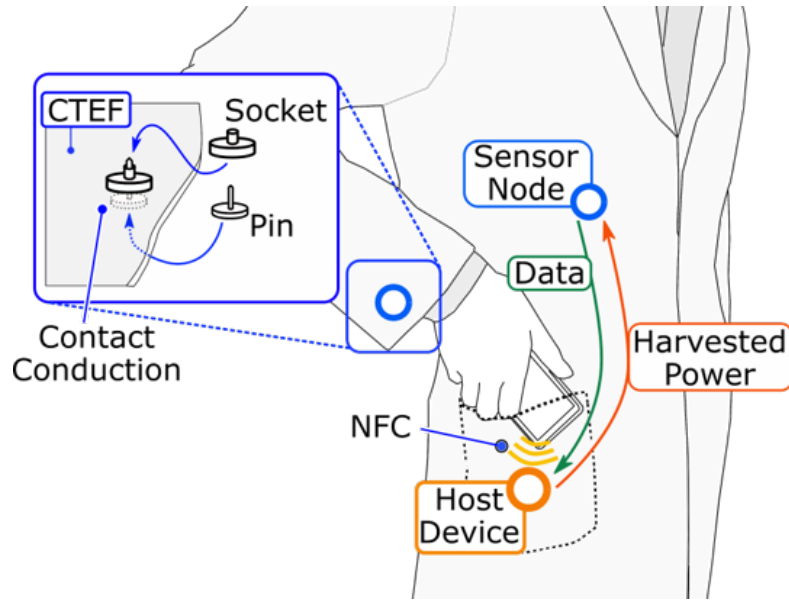
Figure6.3: Concept of power aggregation system by using wearable two-dimensional communication sheet and tack connector.

6.2   Power Aggregation from Multiple Energy Harvesting Device

In this section, we propose a power aggregation scheme from multiple PGEs to the storage terminal without one-to-one wiring by using conductive-thread-embroidered fabric (CTEF) and tack-type connector [40] [41]. Penetration fixing and contact conduction are simultaneously realized at arbitrary positions on the CTEF, as shown in Fig. 6.2. Following are the advantages of our proposal: 1) the amount of power generation can be increased with the number of PGEs, 2) each PGE can be placed at an arbitrary position, and 3) a multi-source EH system can be realized.

In this scheme, the number of PGEs can be adjusted according to the required amount of electricity by simply attaching more PGEs. Free arrangement allows practical installation, such as using PGEs as buttons. Multi-source EH systems increase the types of available energy sources. Moreover, the diversity of EH sources will decrease the fluctuation of generated power due to any changes in environmental conditions.

When PGEs with different output voltages are directly connected in parallel, the output current of the high-voltage PGE flows not only to the storage terminal, but also to the low-voltage PGE, leading to energy loss.

For example, assuming that one of the two solar cells connected in parallel is under shade, which causes the output to lower drastically, the solar cell under shade functions as a diode [48] [49]. Most of the output current of the other solar cell flows to the ground
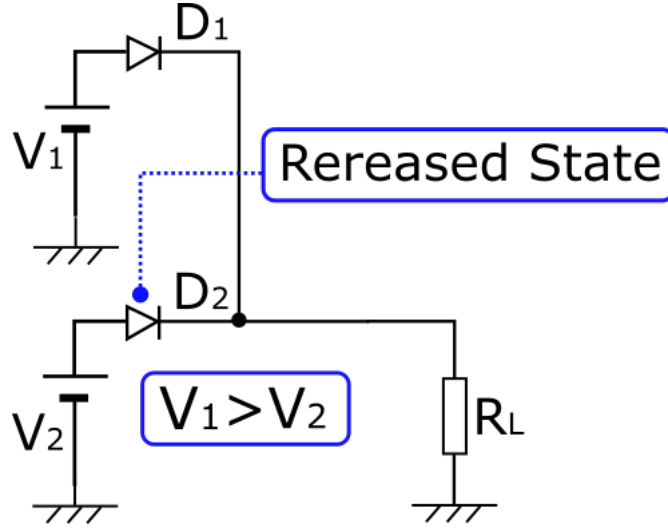
Figure6.4: Maximum value selection circuit.

via the solar cell under shade. In other words, reverse current prevention is necessary for efficient power aggregation.

6.2.1 Power aggregation circuit

In this section, we present a circuit diagram, which aggregates power from multiple PGEs via a CTEF. We also confirm its validity by circuit simulation. The aggregation efficiency is evaluated as the ratio of the charge speed of the storage terminal to the total power generation speed of each PGE. For example, when the total output of the PGEs is 100 mW, with the charging speed of the power storage terminal being 80 mW, the aggregation efficiency is 80%.

As described in above subsection, when the PGEs with different output voltages are directly connected in parallel, the current flows back to the element, decreasing the aggregation efficiency. The diode can stop the reverse current. However, it causes the following problems.

When the two voltage sources V_1,V_2 are connected in parallel to the load R_L via the diodes D_1,D_2, this circuit becomes the maximum value selection circuit, as shown in Fig. 6.4. Assuming $V_1 > V_2$, D_2 experiences a high-impedance state due to the reverse bias, causing the electrical path from V_2 to R_L to break. Thus, even when a large number of PGEs are connected to the CTEF via diodes, only one maximum voltage PGE can be connected to the storage terminal.

The power aggregation circuit proposed in this paper is shown in Fig. 6.5. This circuit has the following two functions: 1) The output of each PGE is temporarily stored in the capacitor C_n (n=1,2,$\cdots$,N); and 2) the temporarily stored energy is transferred to the super capacitor C_{OUT}. The first one is referred to as the temporary power storage function, while
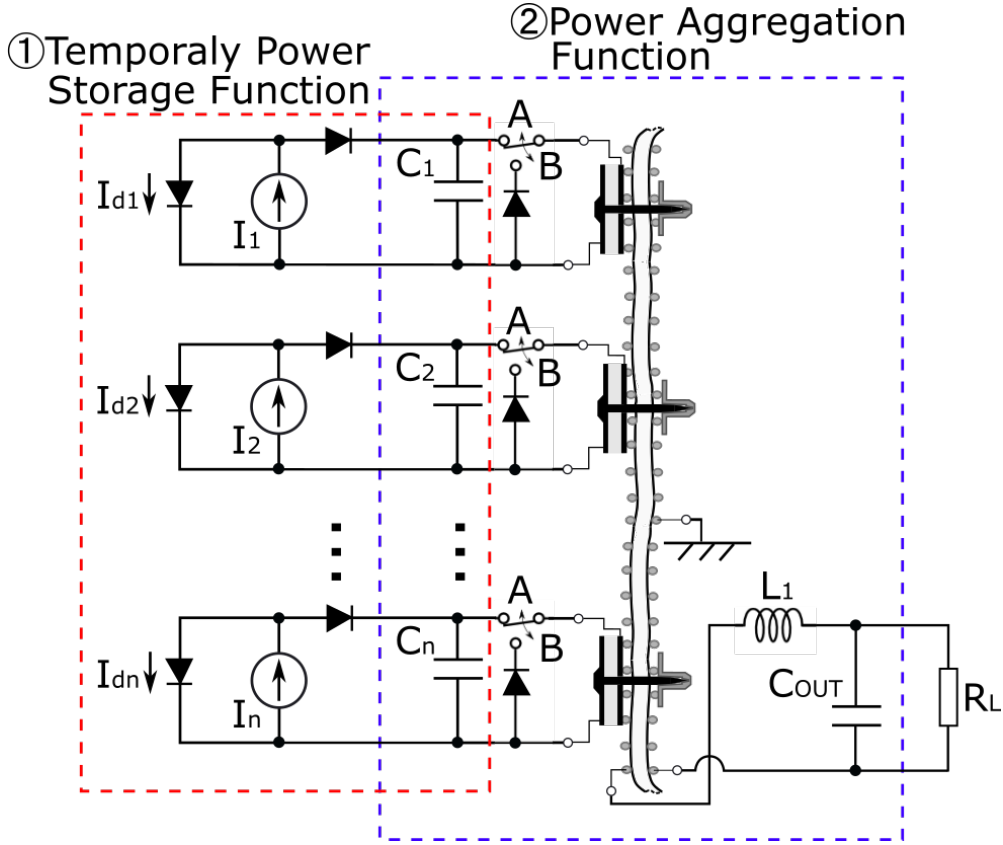
Figure6.5: Schematic diagram of power aggregation circuit.

the other one is referred to as the power aggregation function.

In the temporary power storage function (the switch is turned to B side), each PGE is electrically disconnected from the CTEF. No current flows from other PGEs. In the current aggregation function (switch position A), energy moves from C_n to the coil L_1. After the switch is moved to the B side again, energy flows from L_1 to C_{OUT}.

When capacitors (C_1,C_2) with different voltages are directly connected, some energy is lost by wire resistance through an impulsive current. This is apparent from the following equations.

$$U_{start} = \frac{Q^2_{1\_start}}{2C_1}, \tag{6.1}$$

$$U_{end} = \frac{Q^2_{1\_end}}{2C_1} + \frac{Q^2_{2\_end}}{2C_2}, \tag{6.2}$$

$$= \frac{1}{2C_1}\left(\frac{C_1 Q_{1\_start}}{C_1 + C_2}\right)^2 + \frac{1}{2C_2}\left(\frac{C_2 Q_{1\_start}}{C_1 + C_2}\right)^2, \tag{6.3}$$

$$= \frac{Q^2_{1\_start}}{2 * (C_1 + C_2)}, \tag{6.4}$$

where U_{start} denotes the total energy of C_1 and C_2 when C_2 is empty. Q_{1_start} denotes the charge of C_1 at that time. U_{end} denotes the total energy of C_1 and C_2, when the voltage of both capacitors becomes constant. Q_{1-end}, Q_{2-end} denote the charges of C_1, C_2 at that time. $U_{start} > U_{end}$ indicates the energy loss. If a coil and switch are used between capacitors, $U_{start}=U_{end}$ can be realized, unless switching losses are taken into account.

6.2.2   Circuit simulation

In this subsection, we show the aggregation efficiency of the circuit shown in Fig. 6.5 by circuit simulation with LT SPICE [50]. The number of PGEs and the distribution of each PGE output are changed in the simulation. The PGE is assumed to be a commercially available small solar cell (Sphelar Power Corporation, KSP-F12-12S1P-W1-X [51]). The solar cell is modeled with a current source I_n, generated by light, and a diode current I_{dn} [48] [49]. I_{out_n}, which is the output current of the solar cell, is expressed as:

$$I_{out\_n} = I_n - I_{dn}, \tag{6.5}$$

where

$$I_{dn} = I_o \left\{ \exp \frac{qV_{out\_n}}{nkT} - 1 \right\}, \tag{6.6}$$

where I_o is the reverse saturation current and n denotes the diode performance index. I_o and n depend on the type of solar cell. k is the Boltzmann constant, T is the absolute temperature, q is the elementary charge, and V_{out_n} is the operating voltage.

The aggregation efficiency is the ratio of the charge speed of the storage terminal to the total power generation speed of each PGE. The charge speed is calculated using the capacity and the time derivative of the instantaneous voltage across C_{OUT}. The total power generation speed is calculated using the maximum solar cell output and the number of connected solar cells.

For the control of the switch, we assumed the use of commercially available energy harvest power supply IC (Linear Technology Corporation, LTC3588-1 [52]). The SPICE library, provided by Linear Technology, is used for modeling.

Other parameters used in the simulation are shown in Table 6.1. The values of I_n, I_o and n were determined with reference to the assumed solar cell data sheet [51]. The I-V curve of the solar cell model with the parameters in Table 6.1 is shown in Fig. 6.6. The operating current, at an operating voltage of 6 V, is 2.21 mA. The maximum output is 13.3 mW. This value is used in calculating the total power generation speed.

The SPICE simulation model is shown in Fig. 6.7. The simulation results of the aggregation efficiency for each number of solar cells are shown in Fig. 6.8. When the

Table6.1: Circuit parameters in SPICE simulation.

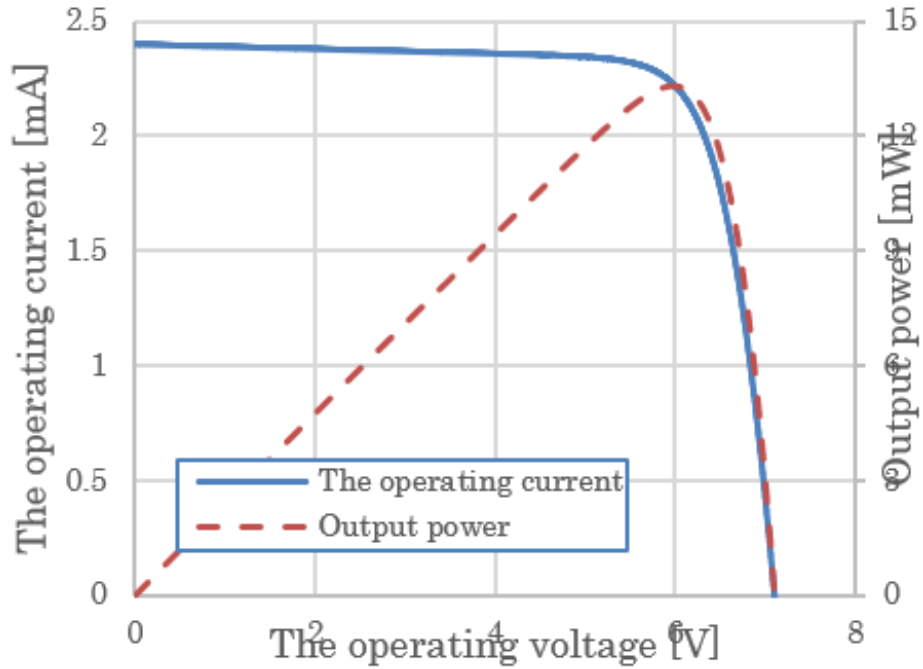|	
I_n	2.4 mA
I_o	$1\ 10^{-13}$ A
n	11.5
C_n	47 μ F
L_1	10 μ H
C_{OUT}	4700 μ F
R_L	250 k Ω

Figure6.6: I-V curve of solar cell simulation model.

number of solar cells is one, the charging speed is 8.3 mW, which is 62.5% of the maximum output of the solar cell. The switching loss and the operating voltage of the solar cell are believed to be the cause of efficiency reduction. The operating voltage is in the range of $3.9-5.1$ V, while the maximum output is obtained at 6 V.

When the number of connected devices increases from 1 to 10, the aggregation efficiency increases from 62.5% to 67.5%. Efficiency is not reduced by increasing the number of devices in this system. Instead, it is advantageous to use several terminals. However, the timing of switching at each device is synchronized in this simulation.

The aggregation efficiency for each dispersion value of output current is shown in Fig. 6.9. The number of connected devices is fixed at 10. The dispersion is adjusted by
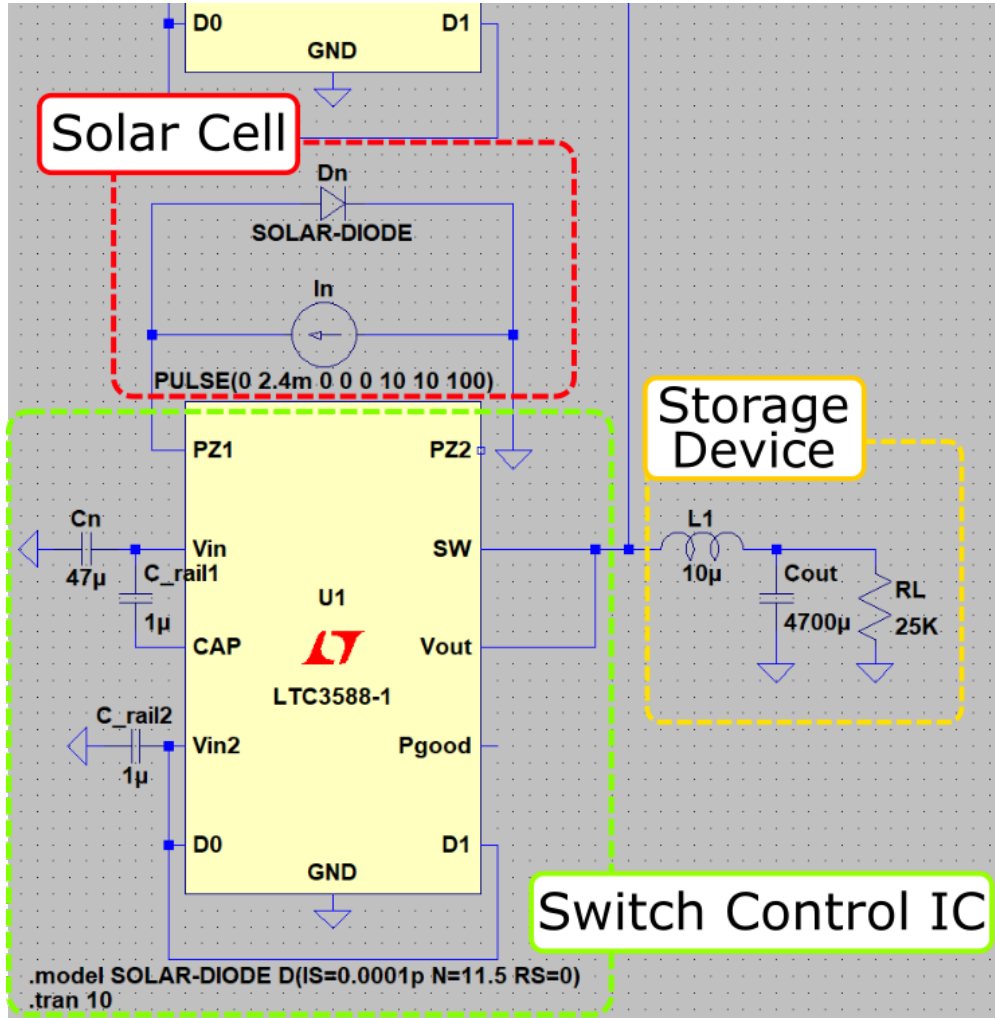
Figure6.7: SPICE simulation model.

changing I_n between 0 and 2.4 mA. When the dispersion increases from 0 mA to 1.45 mA, the aggregation efficiency decreases by 12.3%.

The efficiency is reduced by directly connecting capacitors (C_n) with different voltages via the CTEF. As shown by Eq.6.1 and Eq.6.4, energy loss occurs when capacitors with different voltages are directly connected. Since the power generation speed of each PGE is different, the switching timing varies depending on the device. Thus, the opportunity to directly connect the capacitors with different voltages increases.

6.2.3   Experiment

In this section, we measure and evaluate the charging speed and aggregation efficiency based on the number of devices, by using the prototype EH device. The measurement setup is shown in Fig. 6.10. The prototype EH device is composed of a tack-type connector, a solar cell, and a switch control IC, as shown in Fig. 6.11.
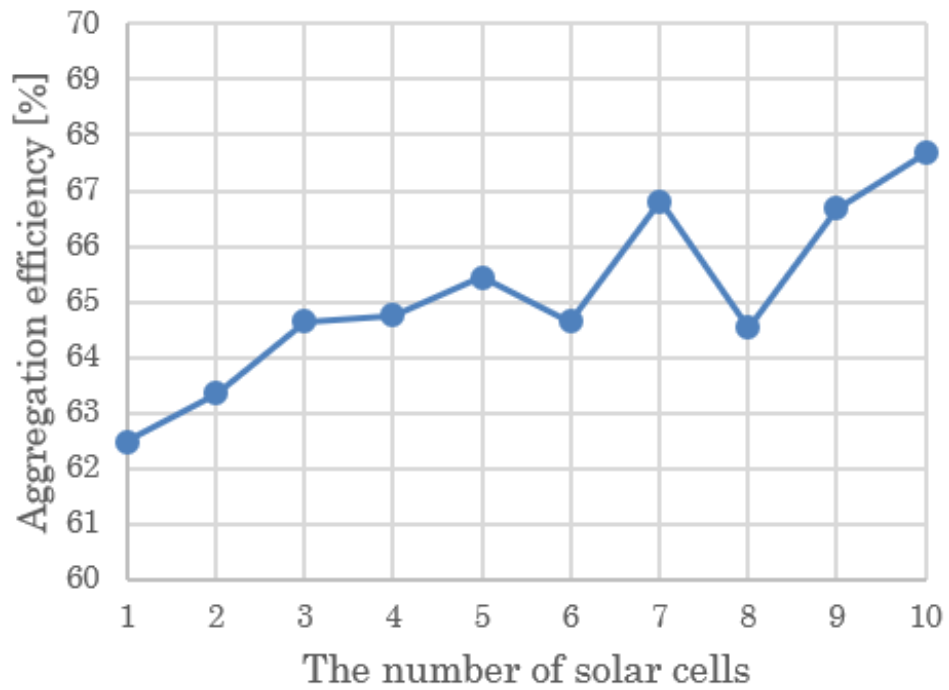
Figure6.8: Aggregation efficiency for each number of solar cells.
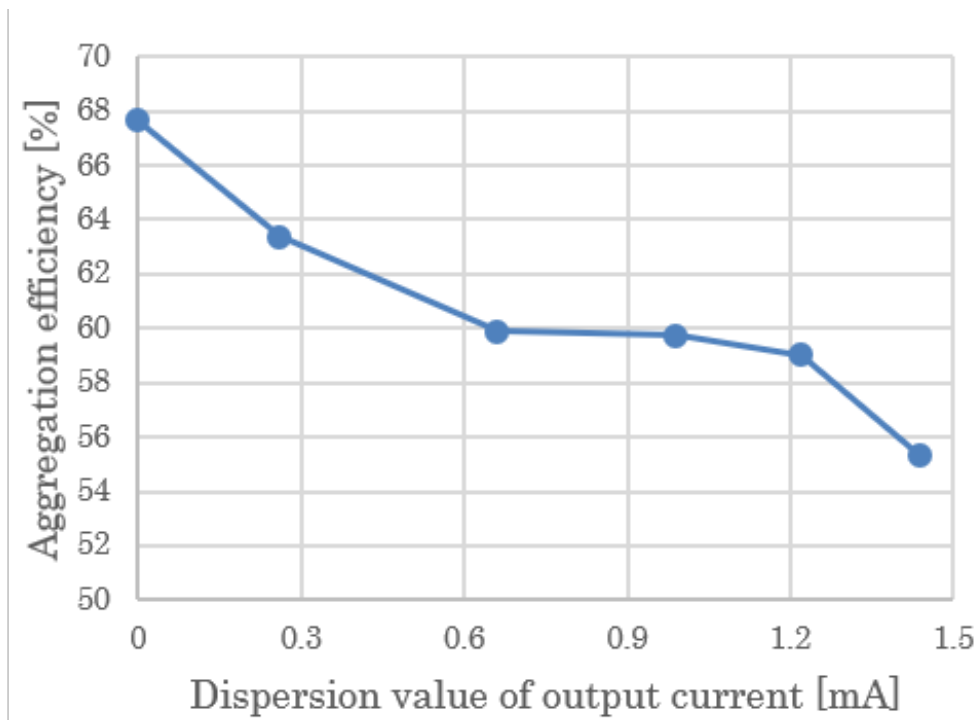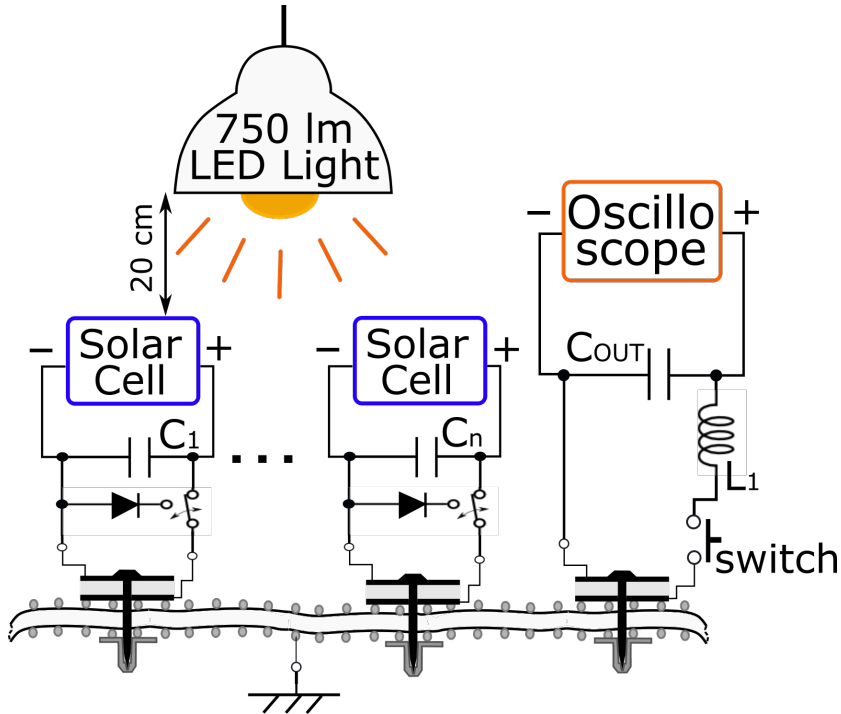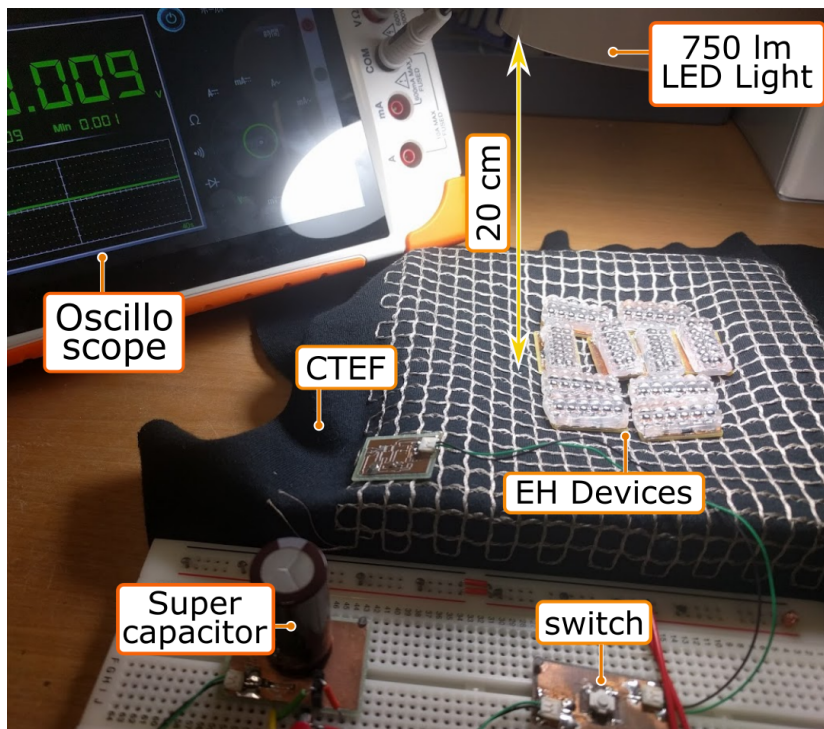

Figure6.9: Aggregation efficiency for each dispersion value of output current.

(a)

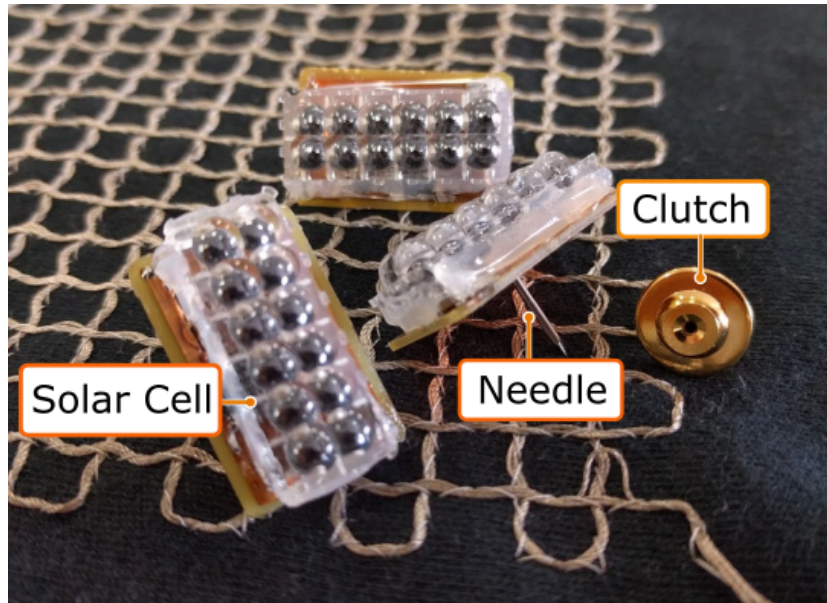(b)

Figure6.10: Simulated results.

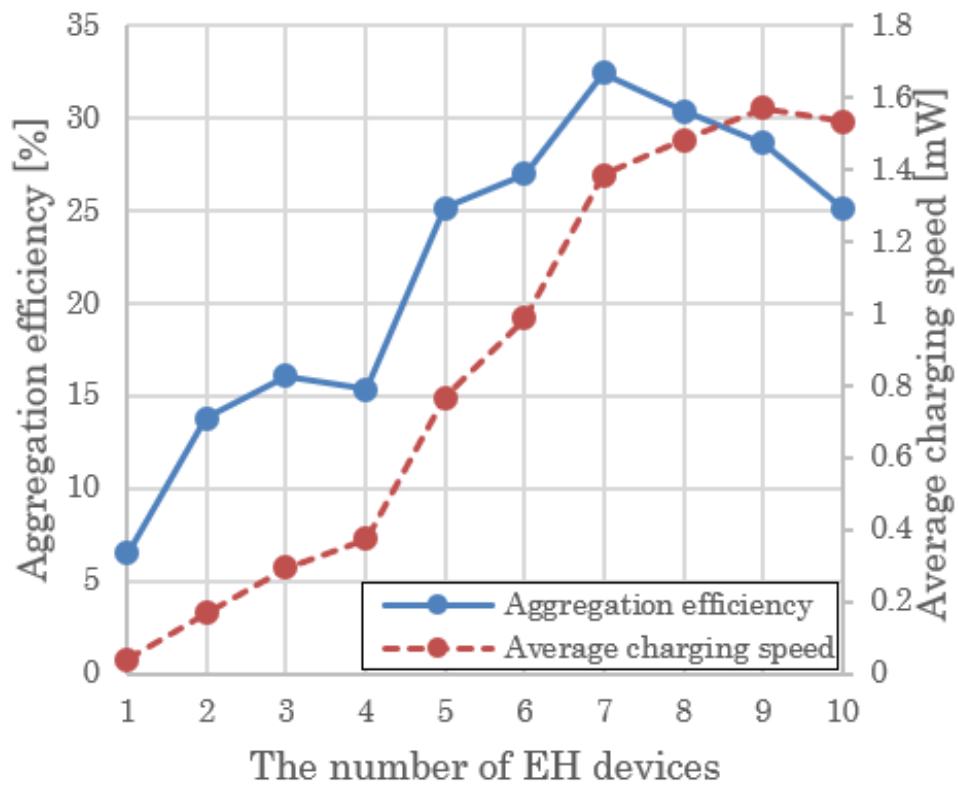Figure6.11: Aggregation efficiency for each dispersion value of output current.

Figure6.12: Aggregation efficiency for each dispersion value of output current.

Each EH device is connected to the CTEF with a tack-type connector. The oscilloscope measures the voltage of the super capacitor every 100 ms. When the switch is pushed, the super capacitor begins to charge. Voltages at five points from the start of charge time to the end time are measured.

The average of the charge speed thus obtained is shown in Fig. 6.12. The aggregation efficiency is also plotted, which is calculated from the average charge speed and the total output power of solar cells. An LED light source of 750 lumens is installed at about 20 cm above the solar cell. The output power of the solar cell varies between 0.6 and 0.7 mW, depending on the position.

The aggregation efficiency begins to show a downward trend when the number of EH devices is 7. As in the simulation result shown in Fig. 6.9, variation in the switching time of the EH devices reduces the efficiency. The charging speed peaks when the number of EH devices is 9. In order to use a larger number of EH devices and increase the charging speed, the energy loss indicated by Eq.6.1 and Eq.6.4 should be prevented. The use of diodes or the synchronization of the switching time at each EH device is an effective solution.

6.3   Body Sensor Networks Powered by an NFC-Coupled Smartphone in the Pocket

In this section, a body sensor networks powered by an NFC-coupled smartphone in the pocket shown in Fig. 6.3 will be described.

NFC-EH requires maintaining antennas within several centimeters to obtain enough power for the host device and sensor nodes. Therefore, the users need to check the direction of a smartphone for positioning of the antennas when putting it in the pocket. And the pocket must be the same size as smartphone to prevent misalignment.

To solve this problem, we propose a host device that can expand the range of NFC-EH by using multiple NFC antennas. Covering the inside of the pocket with multiple NFC antennas does not need the positioning or fixing the smartphone.

6.3.1   Circuit diagram of NFC-coupled host device

we developed a prototype of a NFC-coupled host device that can expand the range of the NFC-EH by increasing the number of NFC antennas. A system model of the host device was shown in Fig. 6.13. We focus the NFC-EH system (red dotted line in Fig. 6.13). The communication system (black line in Fig. 6.13) is still in the concept stage. An I2C communication technology via the CTEF was proposed in [53].

A preliminary experiment was conducted to confirm the range of NFC-EH with one antenna. The received peak-to-peak voltage was measured.
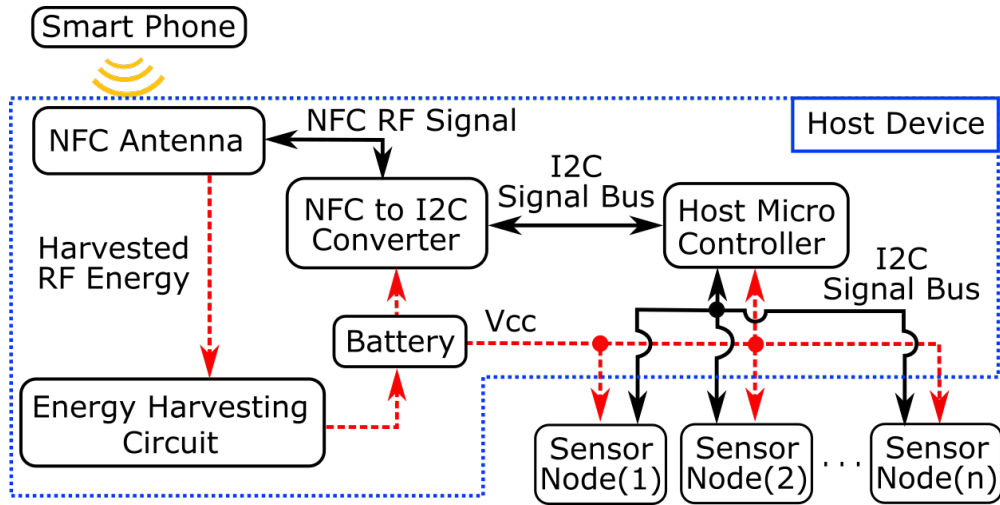
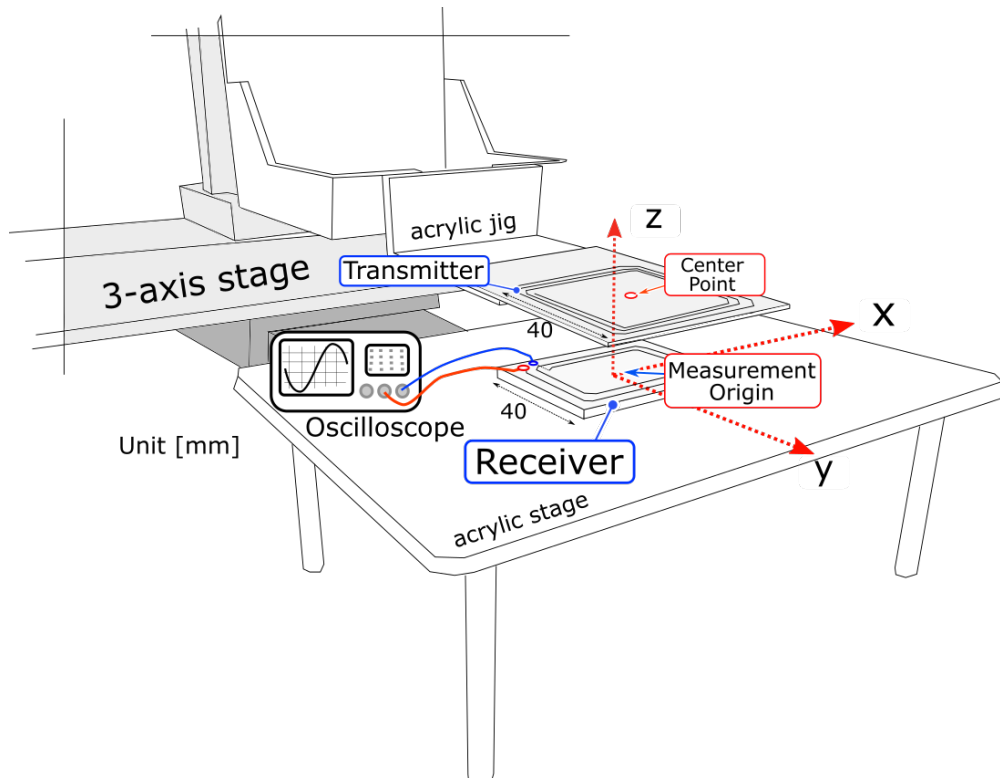Figure6.13: Schematic diagram of measurement setup.

Figure6.14: Preliminary experimental setup.

The experimental setup was shown in Fig. 6.14. The center of the receiving antenna was set as the measure-ment origin. And it fixed to the acrylic stage. The transmitting antenna fixed to the 3-axis stage via an acrylic jig was moved in the y and the z -direction shown in Fig. 6.14.

Fig. 6.15 shows that the received peak-to-peak voltage is halved or less every time the
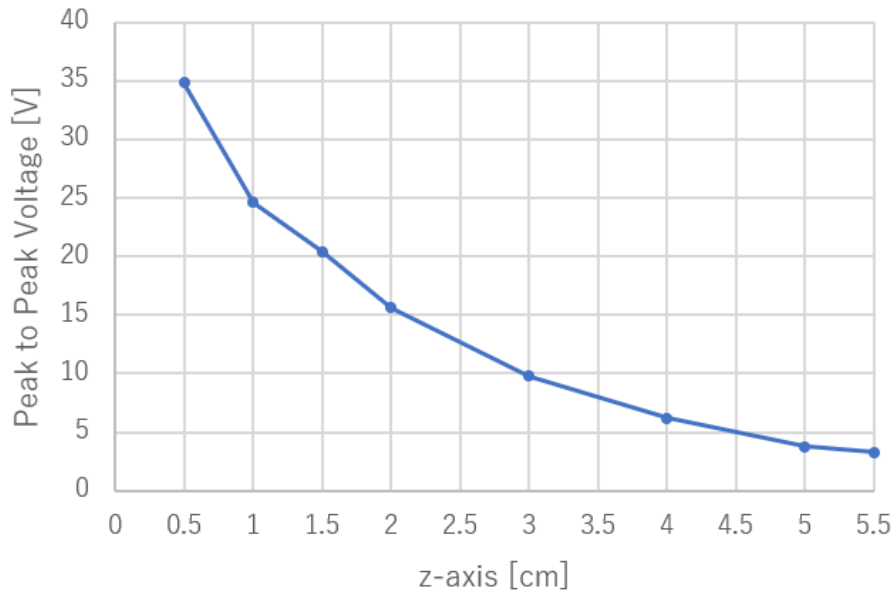
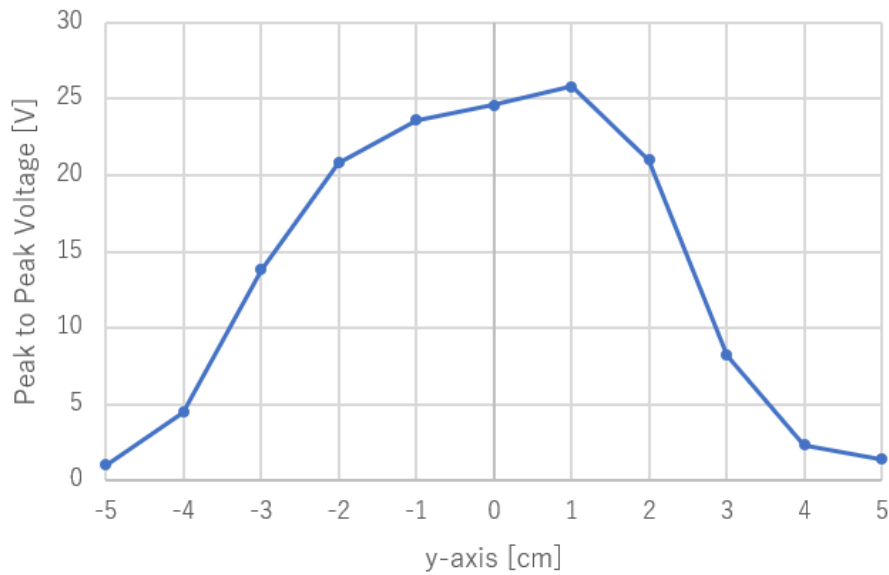Figure6.15: Received peak-to-peak voltage when moving vertically (x = y = 0).

Figure6.16: Received peak-to-peak voltage when moving horizontally (y = 0, z = 1).

distance of z-axis becomes 2 cm apart. Fig. 6.16 shows that the received peak-to-peak voltage sharply decreases with misalignment of antenna width (40 mm) or more.

Next step, the receiving NFC antenna was expanded to two. The experiment was continued by arranging it as shown in Fig. 6.17. The two NFC antennas are connected with the normal polarity and the reverse polarity in series. Fig. 6.18 shows the received peak-to-peak voltage when the transmitting antenna is moved in the y direction.
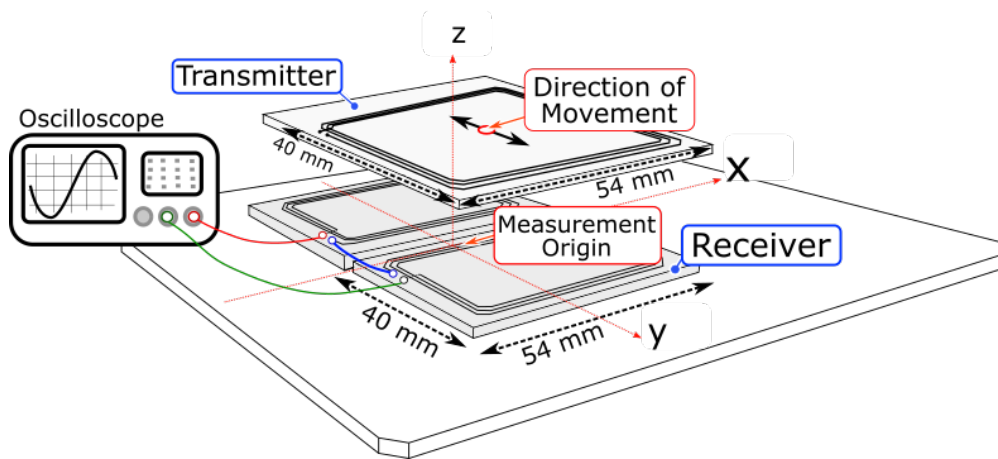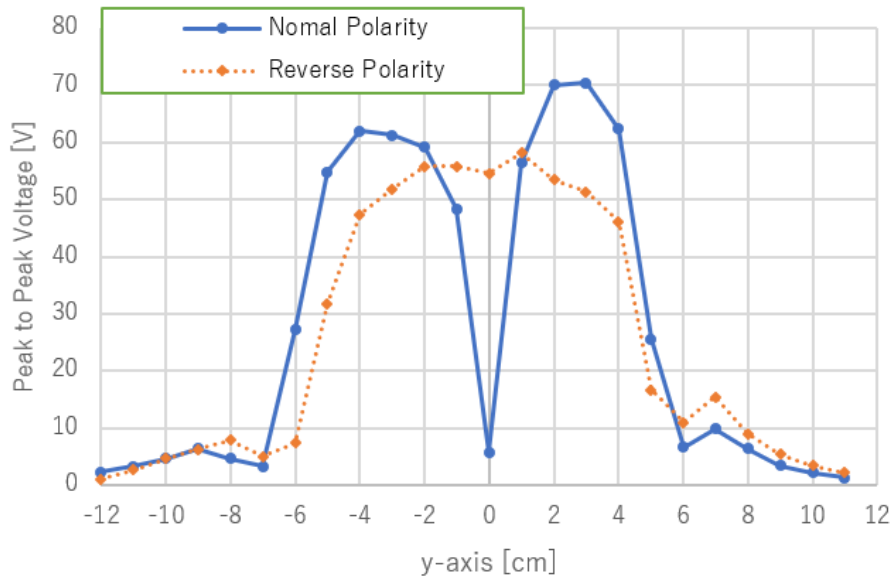
Figure6.17: Experimental setup.

Figure6.18: Received voltage waveform. The transmitter was moved in the y direction with x = 0 cm, z = 1 cm.

The received voltage waveform of each antenna is different in phase and voltage. The energy loss occurs by canceling each other. The result of normal polarity connection shows that a null point occurs when y-axis is 0.

When the one receiving antenna is connected with the opposite polarity, the null point does not occur at the same point. On the other hand, the peak-to-peak voltage of the reverse polarity is lower than the normal polarity when y-axis is from -6 cm to -2 cm or from 2 cm to 6 cm.

To avoid this problem, we use the power aggregation circuit proposed in Section 6.2. The circuit diagram of the proposed host device is shown in Fig. 6.19(a).
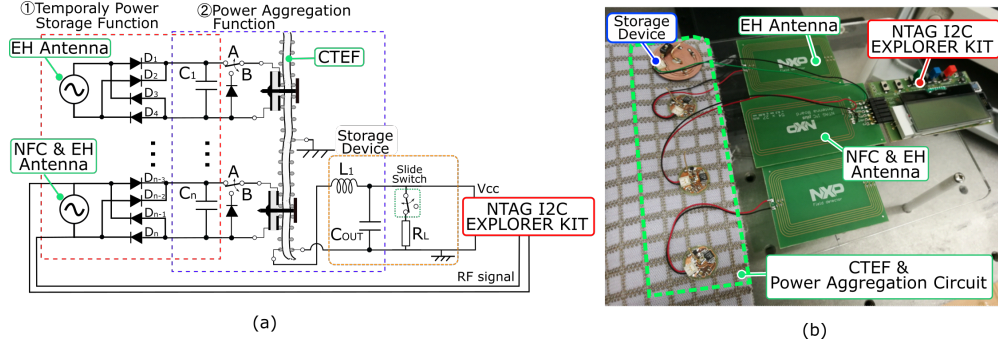
Figure6.19: (a) Circuit diagram of the host device. (b) Prototyped host device.

Notably, the CTEF in the pocket used to connect the antenna is electrically independent of the CTEF of other areas.

The prototyped host device is shown in Fig. 6.19 (b). Each antenna is connected to a pin & socket connector on which a temporary storage capacitor C_1 and switch control IC (LTC3588-1, linear technology [52]) are mounted.

For the communication part, a commercially available development board (NTAG I2C plus Explorer kit, NXP [54]) was used. NTAG I2C converts the NFC signal into an I2C signal and acquires various sensor in-formation on the board via I2C.

6.3.2 Exprtiment

In this section, we evaluate the extension of NFC-EH possible range using multiple antennas and power aggregation circuit. The experimental environment is shown in Fig. 6.20. The measurement origin is the center of the antenna for communication and EH. A charging speed and communication range were measured.

The charging speed W_{charge} is expressed as

$$W_{charge} = \frac{E_{storage}(t_end) - E_{storage}(t_start)}{t_end - t_start}, \tag{6.7}$$

where

$$W_{storage}(t) = \frac{1}{2} C_{out} V^2_{storage}(t), \tag{6.8}$$

$E_{storage}(t)$ denotes the energy charged in C_{out}. And $V_{storage}$ denotes the voltage of C_{out}. t_{start} and t_{end} denote the charging start and end time.

While the slide switch of the storage terminal is turned on, the charge of C_{out} immediately flows to ground through R_L. Thus, the time when the switch is turned off is defined as the charging start time. And the time when the rise of $V_{storage}$ stops is defined as the charging end time. $V_{storage}$ is measured by the oscilloscope.
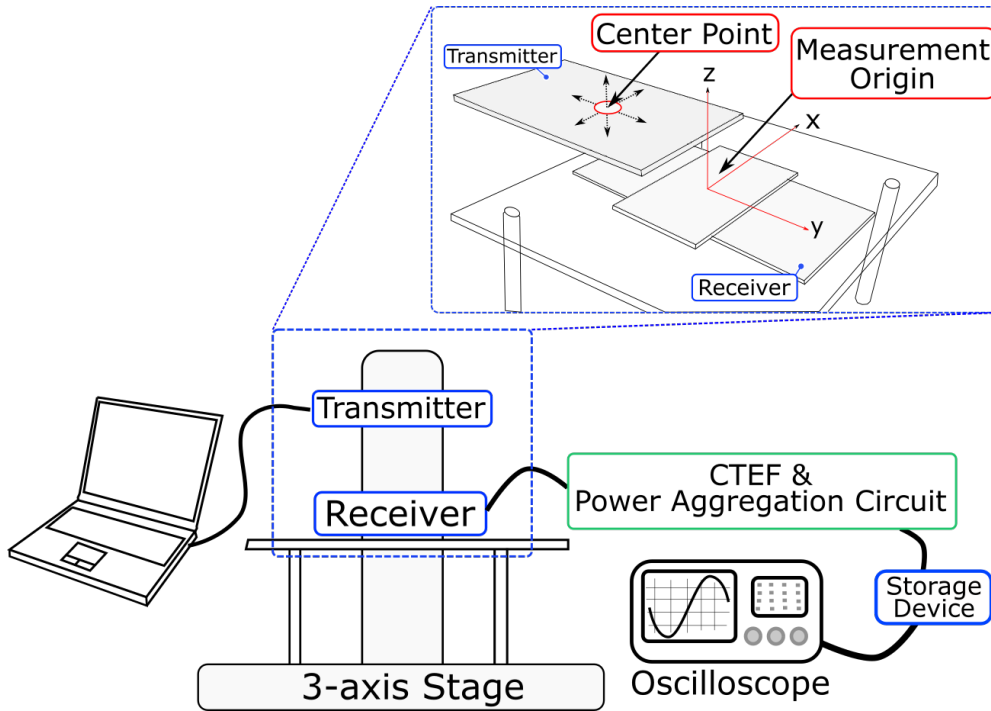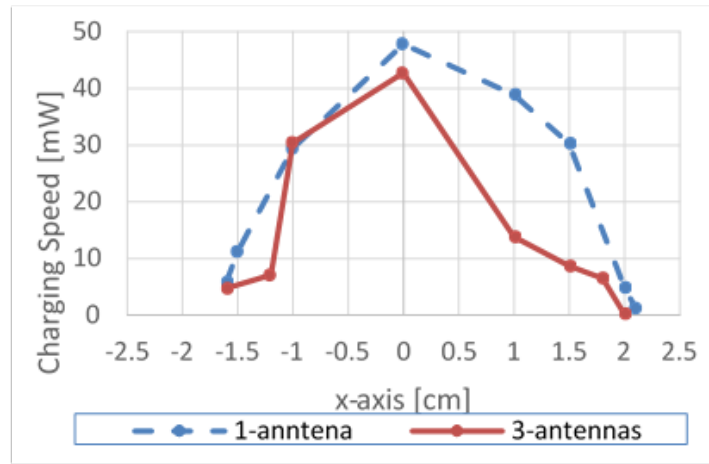
Figure6.20: Experimental setup.

The results of charging speed are shown in the Fig. 6.21. As no antennas were added in the x-axis and z-axis directions, similar results were obtained in the two cases. In the y-axis direction, the distance that can charge 20 mW or more extended from 4 cm to 12 cm. Since the outputs of the adjacent antennas are added, the charging speed has increased more than in the case of one antenna at the boundary between the antennas near $y = \pm 2$ cm

The communication range is defined as the distance until the communication between transmitter and the NTAG Explorer kit is interrupted. It was 2 cm each in the x, y, z direction. While the proposed method extends the range of NFC-EH, the communication range remains un-changed.

6.3.3   Prototyping of entire system

Fig. 6.22 shows a prototype of a host device combining power generation function and NFC function. Sensor data can be read by using NFC tag reading application of smartphone. Each sensor communicates with the host device with I2C protocol. In the prototype system, the CTEF is not used, and the sensor and the host device are individually wired. A system that performs I2C communication with each terminal connected to the conductive cloth has already been proposed. By integrating with this, battery-less BSN with CTEF and I2C protocol can be realized.

(a)
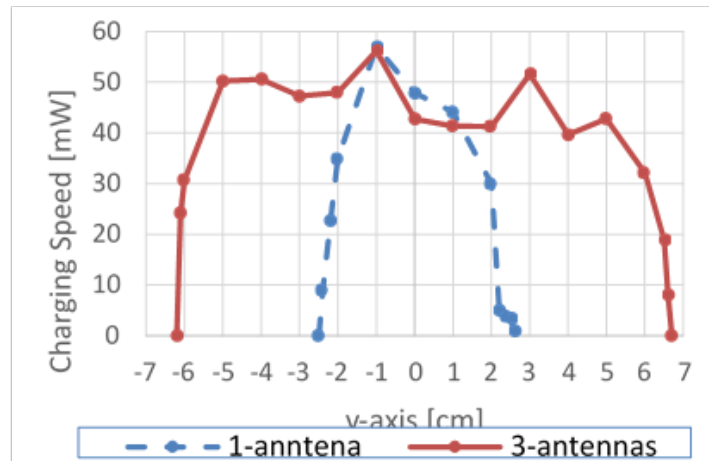
(b)
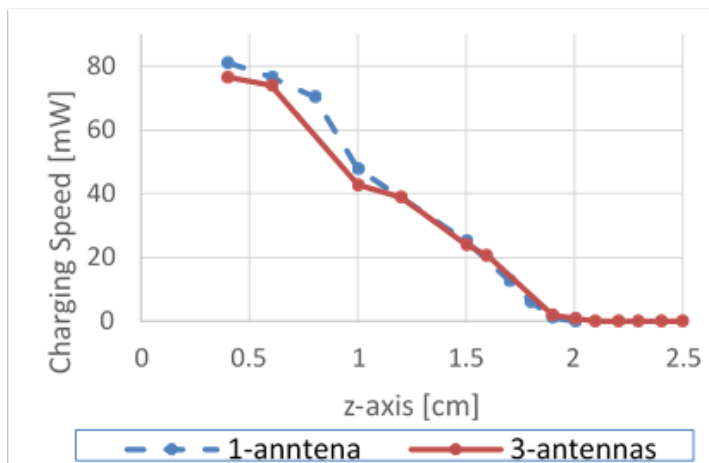
(c)

Figure6.21: Experimental setup.

Figure6.22: prototype of a host device combining power generation function and NFC function.
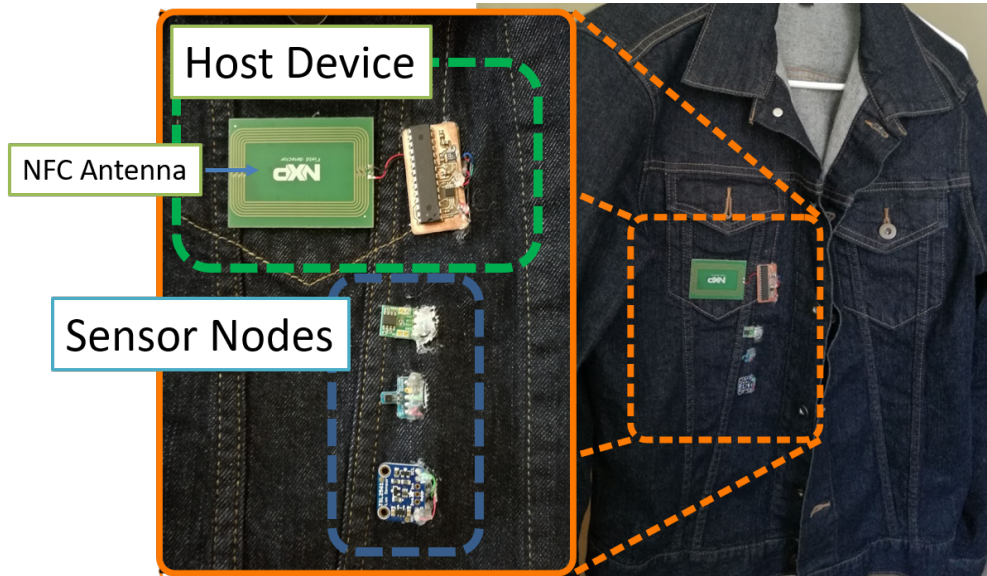
6.3.4   Discussion

We proposed a BSNs scheme which use the NFC-coupled smartphone in the pocket as the power source of a host device and multiple sensor nodes. These devices are wired without one-to-one wiring by using pin & socket type connector and a conductive thread embroidered fabric. The host device and the smartphone are coupled via NFC radio within the pocket. Energy harvesting using NFC radio requires the maintaining NFC antennas within several centimeters. The batteryless host device, which has the power aggregation circuit and multiple NFC antennas, solved the above problem. Positioning and fixing of the smartphone is not required on the area where the multiple antennas are arranged in the pocket.

6.4   Conclusion

In this chapter, we propose two scheme of realizing BSN without batteries. One is that of aggregating electric power generated by multiple EH terminals. The other one is that of recovering electric waves from smart phones in the pocket and generating electricity.

CTEF can realize simple connection without one-to-one wiring. On the other hand, all the elements have constraints to be connected in parallel. we proposed a power aggregation circuit as a scheme for efficiently aggregating electric power from parallelly connected power generation elements with different output voltages.

In a system that collects electric power from smartphones in pockets, we applied the

power aggregation circuit to expand the scope of NFC-EH. Experimental results shows that sufficient power generation is possible regardless of the position of the smartphone in the pocket.

Chapter 7

Conclusion

This thesis presented theoretical analysis, design example, and the feasibility of long-distance WPT system using the sheet-like medium.

In Part I, works on the WPT system were presented.

In Chapter 2, sheet parameters, which is necessary for the discussion in Chapter 3, were obtained with EM field analysis of sheet-like medium. The surface reactance is a key parameter to determine the guided mode. The propagation loss and evanescent field decrease as the reactance decrease.

In Chapter 3, the sheet-like medium and the receiving coupler are represented by an equivalent circuit. The trade-off relationship between the propagation loss and the efficiency when the coupler extracts power from the sheet was described. It was suggested that a sheet surface pattern with high inductivity is required for long distance transmission.

In Chapter 4, a high-inductive surface sheet was proposed. It can realize sufficient reactance at13.56 MHz ISM band. The surface microscopic magnetic field was strengthened due to the zigzag conductor pattern. The estimated maximum efficiency is 84% when the transmission distance is 100-m.

In Part II, energy-efficient wireless communication and battery-less body sensor network using sheet-like medium were presented.

In Chapter 5, we presented the feasibility of high-speed and power-saving wireless communication. By using the method for determining optimal physical layer parameters, more than 100 times higher efficiency than general indoor wireless communication can be achieved. We actually implemented the communication protocol at the software terminal and carried out the experiment.

In Chapter 6, we proposed two scheme of realizing battery-less body sensor networks. One is that of aggregating electric power generated by multiple energy harvesting terminals. The other one is that of harvesting the radio transmitted from the smartphones in the pocket. we proposed a power aggregation circuit as a scheme for efficiently aggregating electric power from parallelly connected power generation elements with different output voltages.

Thus, this work demonstrated the feasibility of the long-distance and high efficient power supply interface. Power supply interface which covers all routes can accelerate the electrification of moving object.

Acknowlegdgement

I would like to express my gratitude for people who helped me to complete this thesis. Firstly, I would like to thank Professor Hiroyuki Shinoda. He is my supervisor and he has given many suggestions for my research throughout the past five years. He is always willing to respect what students have done and gives accurate advice. He always guided me when I faced a difficult problem, and I was able to learn how to think and how to execute to solve the difficulty by myself. Thanks to that, I grew up more than I did before coming to the laboratory.

Secondary, I would like to thank Associate Professor Yasutoshi Makino. He always suggests students challenging propositions and spends a lot of time for research discussions with them. Many lab members, including me, were helped by him.

Thirdly, I am grateful to Akihito Noda. He is now Associate Professor at Nanzan University, and he was Project Researcher in Shinoda-makino laboratory two years ago. He also has given many suggestions and advised me to advance my research. Even if it is holidays, he came to our laboratory and pursued his research. Besides that, no matter how busy he was, he always responded seriously when I asked a question. His advice, which includes gentleness and severity, always inspired me and helped to solve a lot of problems. He is an expert on two-dimensional communication technology which is my research theme. Actually, all my research is based on his research. Without his wonderful work, this research would not have been done.

Keisuke Hasegawa is now Assistant Professor in Nara-laboratory and he was Project Researcher in Shinoda-makino laboratory. His advice and comments have always excited and surprised me to raise my motivation. He is a kind and sincere person, I want to be like him. Masahiro Fujiwara is now Project Researcher in Shinoda-makino laboratory. He is a professional in mathematics and signal processing, and his technical advice was very clear and easy to understand.

From here, I would like to express my gratitude to my colleagues. Takaaki Kamigaki is doctoral students in the same grade and in the same lab. He is a very cheerful and mentally strong person. He frequently faced difficult problems, but he was always confronting them. Sometimes he made weird sounds to reduce his stress, I went easy on him. In addition, I spent a lot of time at the laboratory with Takuro Furumoto and Syun Suzuki. Thanks to these three people I think that I could have enjoyed my research life happily.

Seki Inoue and Akimasa Okada, they have already graduated, but we still have relationships and we often get together for drinking and eating. Even now I am making an electric motorcycle "Magna Zero" with Dr. Inoue and he helped me a lot even at Mini WPT-4WD race. Dr. Okada always encouraged me. He often treated me to an ice cream every time I was depressed. It always energized me.

As is mentioned in above, the interesting and bright people including the professors, are coming every year in Shinoda-makino laboratory and thanks to them, I have been able to enjoy the study and to learn many things.

Finally, I would like to thank my parents. During the past five years, I was able to meet with many excellent people and to have various amazing experiences. It is all thanks to the support of my grateful parents.

Bibliography

[1] O. Y. Edelenbosch, A. F. Hof, B. Nykvist, B. Girod, and D. P. Van Vuuren, "Transport electrification: the effect of recent battery cost reduction on future emission scenarios," Climatic Change, vol. 151, no. 2, pp. 95–108, 2018.

[2] Y. Cao, T. Wang, O. Kaiwartya, G. Min, N. Ahmad, and A. H. Abdullah, "An ev charging management system concerning drivers'trip duration and mobility uncertainty," IEEE Transactions on Systems, Man, and Cybernetics: Systems, vol. 48, no. 4, pp. 596–607, 2018.

[3] A. Pevere, R. Petrella, C. C. Mi, and S. Zhou, "Design of a high efficiency 22 kw wireless power transfer system for evs fast contactless charging stations," in Electric Vehicle Conference (IEVC), 2014 IEEE International, pp. 1–7, IEEE, 2014.

[4] T. Shijo, K. Ogawa, M. Suzuki, Y. Kanekiyo, M. Ishida, and S. Obayashi, "Emi reduction technology in 85 khz band 44 kw wireless power transfer system for rapid contactless charging of electric bus," in Energy Conversion Congress and Exposition (ECCE), 2016 IEEE, pp. 1–6, IEEE, 2016.

[5] S.-H. Lee, B.-S. Lee, and J.-H. Lee, "A new design methodology for a 300-kw, low flux density, large air gap, online wireless power transfer system," IEEE Transactions on Industry Applications, vol. 52, no. 5, pp. 4234–4242, 2016.

[6] I. C. on Non-Ionizing Radiation Protection et al., "Guidelines for limiting exposure to time-varying electric and magnetic fields (1 hz to 100 khz)," Health physics, vol. 99, no. 6, pp. 818–836, 2010.

[7] H. Shinoda, Y. Makino, N. Yamahira, and H. Itai, "Surface sensor network using inductive signal transmission layer," in Fourth International Conference on Networked Sensing Systems, pp. 201–206, IEEE, 2007.

[8] N. Shinohara and N. Kamiyoshikawa, "Study of flat beam in near-field for beam-type wireless power transfer via microwaves," in Antennas and Propagation (EUCAP), 2017 11th European Conference on, pp. 780–782, IEEE, 2017.

[9] W. C. Brown, "The history of power transmission by radio waves," IEEE Transactions on microwave theory and techniques, vol. 32, no. 9, pp. 1230–1242, 1984.

[10] N. Shinohara, "Power without wires," IEEE Microwave Magazine, vol. 12, no. 7, pp. S64–S73, 2011.

[11] S. Ho, J. Wang, W. Fu, and M. Sun, "A comparative study between novel witricity

and traditional inductive magnetic coupling in wireless charging," IEEE Transactions on Magnetics, vol. 47, no. 5, pp. 1522–1525, 2011.

[12] J. Shin, S. Shin, Y. Kim, S. Ahn, S. Lee, G. Jung, S.-J. Jeon, and D.-H. Cho, "Design and implementation of shaped magnetic-resonance-based wireless power transfer system for roadway-powered moving electric vehicles," IEEE Transactions on Industrial electronics, vol. 61, no. 3, pp. 1179–1192, 2014.

[13] A. Kurs, A. Karalis, R. Moffatt, J. D. Joannopoulos, P. Fisher, and M. Soljačić, "Wireless power transfer via strongly coupled magnetic resonances," science, vol. 317, no. 5834, pp. 83–86, 2007.

[14] A. Noda and H. Shinoda, "Selective wireless power transmission through high-q flat waveguide-ring resonator on 2-d waveguide sheet," IEEE transactions on microwave theory and techniques, vol. 59, no. 8, pp. 2158–2167, 2011.

[15] A. Noda, A Study on Safe Power Transmission Using Two-Dimensional Waveguide. PhD thesis, The University of Tokyo, 2013.

[16] N. Yamahira, Y. Makino, H. Itai, and H. Shinoda, "Proximity connection in two-dimensional signal transmission," in 2006 SICE-ICASE International Joint Conference, pp. 2735–2740, 2006.

[17] T. Ohira, "Via-wheel power transfer to vehicles in motion," in Wireless Power Transfer (WPT), 2013 IEEE, pp. 242–246, IEEE, 2013.

[18] T. Ohira, "A battery-less electric roadway vehicle runs for the first time in the world," in Microwaves for Intelligent Mobility (ICMIM), 2017 IEEE MTT-S International Conference on, pp. 75–78, IEEE, 2017.

[19] S. Sakihara, S. Kitabayashi, N. Sakai, and T. Ohira, "Far-end reactor matching to a traveling load along an RF power transmission line," IEICE Transactions on Fundamentals of Electronics, Communications and Computer Sciences, vol. E101A, no. 2, pp. 396–401, 2018.

[20] T. Ohira, "Angular expression of maximum power transfer efficiency in reciprocal two-port systems," in Wireless Power Transfer Conference (WPTC), 2014 IEEE, pp. 228–230, IEEE, 2014.

[21] D. Halperin, B. Greenstein, A. Sheth, and D. Wetherall, "Demystifying 802.11 n power consumption," in Proceedings of the 2010 international conference on Power aware computing and systems, p. 1, 2010.

[22] 猿渡俊介 and 渡辺尚, "ビッグデータを生み出せない無線センサネットワーク," 計測と制御, vol. 52, no. 11, pp. 973–979, 2013.

[23] "http://www.sony.net/sonyinfo/news/press/201202/12-027e/,"

[24] M. of Internal Affairs and Communications, "Regulation of the extremely low power radio station," http://www.tele.soumu.go.jp/e/ref/ material/rule/.

[25] A. Noda and H. Shinoda, "Active tile for room-size uwb 2-d communication," in

System Integration (SII), 2015 IEEE/SICE International Symposium on, pp. 668–671, IEEE, 2015.

[26] A. Okada, A. Noda, and H. Shinoda, "Time domain characteristics of multiple uwb 2d communication tiles," in System Integration (SII), 2015 IEEE/SICE International Symposium on, pp. 817–822, IEEE, 2015.

[27] B. Kellogg, V. Talla, S. Gollakota, and J. R. Smith, "Passive wi-fi: Bringing low power to wi-fi transmissions.," in NSDI, vol. 16, pp. 151–164, 2016.

[28] A. Noda and H. Shinoda, "Wireless lan on 2-d communication tiles using ultra-wideband as an alternative spectrum resource," in Ubiquitous Wireless Broadband (ICUWB), 2015 IEEE International Conference on, pp. 1–6, IEEE, 2015.

[29] R. v. Nee and R. Prasad, OFDM for wireless multimedia communications. Artech House, Inc., 2000.

[30] C. E. Shannon, "A mathematical theory of communication," Bell system technical journal, vol. 27, no. 3, pp. 379–423, 1948.

[31] Y. Karasawa, T. Kuroda, and H. Iwai, "The equivalent transmission-path model-a tool for analyzing error floor characteristics due to intersymbol interference in nakagami-rice fading environments," IEEE transactions on vehicular technology, vol. 46, no. 1, pp. 194–202, 1997.

[32] Y. Karasawa and H. Iwai, "Enhancement of the etp model: How to calculate ber due to isi for wide-band digital transmission in nakagami-rice fading environments," IEEE transactions on vehicular technology, vol. 49, no. 6, pp. 2113–2120, 2000.

[33] K. Y, Radiowave propagation fundamentals for digital mobile communications(Second edition). CORONA PUBLISHING, Inc., 2011.

[34] H. Bogucka and A. Conti, "Degrees of freedom for energy savings in practical adaptive wireless systems," IEEE Communications Magazine, vol. 49, no. 6, 2011.

[35] G. Radio, "The free & open software radio ecosystems," in http://gnuradio.org/, IEEE.

[36] Y. Masuda, A. Noda, and H. Shinoda, "A low power and high speed data transmission system based on 2D communication," IEICE Communications Express, vol. 1, no. 9, pp. 322–328, 2013.

[37] A. Nadeem, M. A. Hussain, O. Owais, A. Salam, S. Iqbal, and K. Ahsan, "Application specific study, analysis and classification of body area wireless sensor network applications," Computer Networks, vol. 83, pp. 363–380, 2015.

[38] P. Gope and T. Hwang, "Bsn-care: A secure iot-based modern healthcare system using body sensor network," IEEE Sensors Journal, vol. 16, no. 5, pp. 1368–1376, 2016.

[39] F. Albinali, S. Intille, W. Haskell, and M. Rosenberger, "Using wearable activity type detection to improve physical activity energy expenditure estimation," in Proceedings

of the 12th ACM international conference on Ubiquitous computing, pp. 311–320, ACM, 2010.

[40] A. Noda, Y. Tajima, and H. Shinoda, "Multiplex wireless power transfer to actuators distributed on flexible 2-d communication sheet for wearable tactile display," in Proc. the 17th SICE System Integration Division Annual Conference, pp. 1349–1353, 2016.

[41] A. Noda and H. Shinoda, "Frequency-division-multiplexed signal and power transfer for wearable devices networked via conductive embroideries on a cloth," in Microwave Symposium (IMS), 2017 IEEE MTT-S International, pp. 537–540, IEEE, 2017.

[42] M.-l. Ku, W. Li, Y. Chen, S. Member, and K. J. R. Liu, "Advances in Energy Harvesting Communications : Past , Present , and Future Challenges," vol. 18, no. 2, pp. 1384–1412, 2016.

[43] M. Magno and D. Boyle, "Wearable energy harvesting: From body to battery," in Design & Technology of Integrated Systems In Nanoscale Era (DTIS), 2017 12th International Conference on, pp. 1–6, IEEE, 2017.

[44] P. Spies, M. Pollak, and L. Mateu, Handbook of energy harvesting power supplies and applications. CRC Press, 2015.

[45] A. S. Weddell, M. Magno, G. V. Merrett, D. Brunelli, B. M. Al-Hashimi, and L. Benini, "A survey of multi-source energy harvesting systems," in Design, Automation & Test in Europe Conference & Exhibition (DATE), 2013, pp. 905–908, IEEE, 2013.

[46] V. Coskun, B. Ozdenizci, and K. Ok, "A survey on near field communication (nfc) technology," Wireless personal communications, vol. 71, no. 3, pp. 2259–2294, 2013.

[47] J. R. Smith, "NFC-WISP : A Sensing and Computationally Enhanced Near-Field RFID Platform," pp. 174–181, 2015.

[48] K. T and E. S, "Simulated power source based on output characteristics of solar cell," IEEJ Trans. Industry Applications, vol. 113, no. 6, pp. 753–759, 1993.

[49] L. M. Fraas and L. D. Partain, Solar cells and their applications, vol. 236. John Wiley & Sons, 2010.

[50] L. Technology, "Ltspice," pp. http://www.linear–tech.co.jp/designtools/software/#LTspice.

[51] S. Power, "Array f12," in http://akizukidenshi.com/download/ds/akizuki/j35881fa.pdf.

[52] L. Technology, "Ltc3588-1," in http://akizukidenshi.com/download/ds/akizuki/j35881fa.pdf.

[53] A. Noda and H. Shinoda, "I2c-enabled batteryless sensors on double-layered conductive fabric," in Proceedings of the 15th IEEE Conference on Body Sensor Networks, Las Vegas, NV, USA, p. 1, 2018.

[54] NXP, "Ntag i2c plus explorer kit,"

発表文献

[1] 増田祐一, 野田聡人, 岡田明正, 牧野泰才, 篠田裕之, "2次元通信タイル間接続のための近接コネクタ," 第 15 回計測自動制御学会システムインテグレーション部門講演会, 2015.

[2] 増田祐一, 野田聡人, 篠田裕之, "二次元通信タイル間接続の為の近接カプラの試作," ロボティクス・メカトロニクス講演会 (ROBOMECH) 2015, 2015.

[3] 増田祐一, 野田聡人, 岡田明正, 福井雄大, 篠田裕之, "二次元通信タイルを介した多視点カメラシステム," 第 16 回計測自動制御学会システムインテグレーション部門講演会, 2015.

[4] 増田祐一, 野田聡人, 篠田裕之, "二次元通信環境における低消費電力・高速無線通信," 2016 年電子情報通信学会総合大会, 2016.

[5] 増田祐一, 野田聡人, 篠田裕之, "二次元通信環境を用いた高速・微弱電力信号伝送," 第 33 回センシングフォーラム, 2016.

[6] 増田祐一, 野田聡人, 篠田裕之, "二次元通信環境を活用した高速・微弱電力信号伝送における物理層設計," 第 17 回計測自動制御学会システムインテグレーション部門講演会, 2016.

[7] 増田祐一, 野田聡人, 篠田裕之, "二次元通信環境における高速・省電力信号伝送のための物理層設計," 電子情報通信学会技術研究報告 SRW 短距離無線通信研究会, 2017.

[8] 増田祐一, 野田聡人, 篠田裕之, "二次元通信パッドを用いた TransferJet 通信範囲の拡大による近距離高速無線信号伝送," 電子情報通信学会技術研究報告 SRW 短距離無線通信研究会, 2017.

[9] 増田祐一, 野田聡人, 篠田裕之, "ウェアラブル二次元通信を用いた電力集約," 第 34 回センシングフォーラム, 2017.

[10] 増田祐一, 野田聡人, 篠田裕之, "ウェアラブル二次元通信シートと NFC 対応ホスト端末を用いた Batteryless Body Sensor Networks," 電子情報通信学会技術研究報告 SRW 短距離無線通信研究会, 2018.

[11] 増田祐一, 野田聡人, 篠田裕之, "二次元通信技術を用いた走行中無線給電," 2018 年電子情報通信学会ソサイエティ大会, 2018.

[12] Yuichi Masuda, Akihito Noda, and Hiroyuki Shinoda, "Contactless Coupler for 2D Communication Tile Connection," in Proceedings of SICE Annual Conference 2015, 2015.

[13] Akihito Noda, Akimasa Okada, Yudai Fukui, Yuichi Masuda and Hiroyuki Shinoda, "Massive Multiple Access Wireless LAN Using Ultra-Wideband Waveguide Floor Tiles," in Proceedings of the 2016 13th Annual IEEE Consumer Communications and Networking Conference (CCNC), 2016.

[14] Yuichi Masuda, Akihito Noda, Hiroyuki Shinoda, "Physical Layer Design of Energy-Efficient Data Transmission in 2D Communication Environments," in Proceedings of IEEE VTC fall 2017, 2017.

[15] Yuichi Masuda, Akihito Noda, Hiroyuki Shinoda, "Power Aggregation from Multiple Energy Harvesting Devices Via a Conductive Embroidered Cloth," in Proceedings of IEEE/SICE International Symposium on System Integration, 2017.

[16] Yuichi Masuda, Akihito Noda, Hiroyuki Shinoda, "Whole Body Human Power-Based Energy Harvesting using a Conductive Embroidered Cloth and a Power Aggregation Circuit," in Proceedings of IEEE 15th International Conference on Wearable and Implantable Body Sensor Networks (BSN), 2018.

[17] Yuichi Masuda, Akihito Noda and Hiroyuki Shinoda, "Body Sensor Networks by an NFC-coupled Smartphone in the Pocket," in Proceedings of 40th Annual International Conference of the IEEE Engineering in Medicine and Biology Society (EMBC), 2018.

[18] Yuichi Masuda, Akihito Noda and Hiroyuki Shinoda, "A low power and high speed data transmission system based on 2D communication," IEICE Communications Express (ComEX), 2016.

受賞等

[1] 第 15 回 SICE SI2014 優秀講演賞. 増田祐一, 野田聡人, 岡田明正, 牧野泰才, 篠田裕之: "2次元通信タイル間接続のための近接コネクタ," 第 15 回計測自動制御学会システムインテグレーション部門講演会, 2015.

[2] SICE Annual Conference International Award of the SICE2014. Yuichi Masuda, Akihito Noda, and Hiroyuki Shinoda: "Contactless Coupler for 2D Communication Tile Connection," 2014 IEEE SICE Annual Conference, 2014.

[3] 研究科長賞. 増田祐一, "" 東京大学大学院新領域創成科学研究科, 2016.

[4] 2016 年度短距離無線通信研究会優秀学生賞. 増田祐一, 野田聡人, 篠田裕之, "二次元通信環境における高速・省電力信号伝送のための物理層設計," 電子情報通信学会技術研究報告 SRW 短距離無線通信研究会, 2017.

[5] 2016 年度短距離無線通信研究会論文賞. 野田聡人, 増田祐一, 篠田裕之, "二次元通信タイルを介した微弱無線相当の高速室内ネットワーク," 電子情報通信学会技術研究報告 SRW 短距離無線通信研究会, 2017.

[6] 特許出願, 出願人: 国立大学法人東京大学, 発明者: 増田祐一, 篠田裕之, "二次元無線給電シート、二次元無線給電システム、及び敷設方法," , 2018.